Construction and Building Materials 458 (2025) 139542

Contents lists available at ScienceDirect

Construction and Building Materials

journal homepage: www.elsevier.com/locate/conbuildmat

Self-healing efficiency of sustainable biochar-cement composites incorporating crystalline admixtures

Xuqun Lin [a], Quang Dieu Nguyen [a,*], Arnaud Castel [a], Peiran Li [b], Vivian W.Y. Tam [b], Wengui Li [c]

[a] School of Civil and Environmental Engineering, University of Technology Sydney, NSW 2007, Australia
[b] School of Engineering, Design of Built Environments, Westen Sydney University, NSW 2751, Australia
[c] Centre for Infrastructure Engineering and Safety, School of Civil and Environmental Engineering, The University of New South Wales, NSW 2052, Australia

ARTICLE INFO

Keywords:
Self-healing concrete
Crystalline admixtures
Biochar
Nuclear Magnetic Resonance (NMR)
Self-healing product
SEM-EDS
Image analysis
FTIR
XRD
Self-healing products

ABSTRACT

Concrete is vulnerable to cracking due to its low tensile strength and brittle nature. Cracks contribute to accelerate the penetration of aggressive ions such as chlorides into the cementitious matrix potentially leading to steel reinforcement corrosion. Self-healing concrete has been identified as a potential solution to eliminate the effect of cracks, helping to reduce the high costs related to repairing deteriorating structures. Although many studies were conducted using General Purpose cement (GPC) or blended cement-based materials, only a very limited number of studies attempted to assess the self-healing behaviour of cementitious composites incorporating biochar. This study investigates the combined effects of wood biochar, partially replacing GPC, and crystalline admixture (CA) on the self-healing performance of biochar-cement composites. Three-point bending loading was conducted to create cracks. Cracked samples were exposed to either dry condition, permanent water immersion, or wetting/drying cycles in water. Cracks self-healing was evaluated using both optical microscopy and binary image analysis. The self-healing products were analysed using SEM-EDS, XRD, TG, FTIR, and NMR. Wetting/drying cycles in water was the most effective exposure condition allowing to totally heal the cracks of CA and CA-Biochar specimens. The microstructural analysis confirmed the formation of calcite and portlandite in the healing products. FTIR and NMR spectra confirmed the formation of limited amounts of C-S-H gel. Biochar particle provided more nucleation sites for the self-healing process, healing wider crack width than in cementitious composites containing only CA.

1. Introduction

Cementitious composites are brittle and vulnerable to cracking due to restrained loads, shrinkage, and environmental factors, such as wind or temperature varieties [1]. As a result, aggressive ions ingress, such as chlorides, is accelerated to induce steel bar corrosion [2], leading to strength degradation and loss of serviceability [3–5]. More importantly, repairing crack-related damage in concrete structures requires significant cost, estimated at $13 billion annually for damaged structure repairing in Australia [6] and $78 - $112 billion for bridge deficiency repairing in USA [5,7]. Hence, timely crack control is highly desirable to repair or heal the cracks before leading to both strength loss and service life reduction. As a result, numerous studies were conducted to understand and develop the self-healing concept, referring to stimulated crack repairing by self-healing agent without additional material or labour costs [8–12]. Among different self-healing agents, such as vascular network [11], microcapsule-based agent [13–15], and mineral admixtures [16–19], crystalline admixtures (CA) have attracted significant research attention.

Although CA is a commercial product utilised as a permeability-reducing agent [20,21], several studies has reported that CA could effectively improve the autogenous self-healing of CA-cement composites [22–28]. Lin et al. [19] reported that CA could induce different self-healing products repairing the cracks, including carbonate precipitation (calcium carbonate) [29,30] and complex precipitation (C-S-H gel and insoluble deposit M_xCaR_x-$(H_2O)_x$) [31,32]. Furthermore, CA could also effectively heal cracks in cementitious composites under aggressive curing environments, such as chloride solution [33,34], seawater [35,36], and freeze-thaw cycle [37,38]. Furthermore, CA improves the durability properties of CA-cement composites, including lower water

* Corresponding author.
E-mail address: quangdieu.nguyen@uts.edu.au (Q.D. Nguyen).

https://doi.org/10.1016/j.conbuildmat.2024.139542
Received 1 October 2024; Received in revised form 25 November 2024; Accepted 9 December 2024
Available online 12 December 2024

permeability [39–41], shrinkage reduction [42], and higher chloride-ion resistance [38,43–46]. It should be noted that most of self-healing studies incorporating CA are carried out using plain OPC cement. However, sustainable concrete design requires low carbon footprint of the cement-based structures, and a feasible strategy is to partially replace cement with different supplementary cementitious materials (SCMs), such as FA or slag [47,48], waste glass powder [49,50], and biochar [51–53].

Thimmareddy et al. [54] observed that 1.1 wt% CA addition led to complete crack closure in the cementitious samples with 20 wt% fly ash (FA) after 42 days. Cappellesso et al. [26] found that 0.8 wt% CA promoted the crack closure of slag-cement ultra-high performance concrete at second crack healing cycle, and the main self-healing products were calcium carbonate and C-S-H gels. Li et al. [55] concluded that slag-cement samples with 1.2 wt% CA had higher crack closure rate than CA-free samples after 56 days, and 10 wt% slag was the optimal dosage to replace cement. CA could improve the self-healing performance of low-carbon cementitious composites incorporating SCMs, such as slag, FA, and metakaolin. Yet, there is no current literature investigating the self-healing behaviour of biochar-cement composites, limiting its practical application in the self-healing concrete. Many studies [51,56–58] reported that biochar could promote both mechanical and durability properties of biochar-cement composites, while mitigating the carbon footprint of burning biomass and cement manufacturing. Adding 2 wt% olive tree biochar in biochar-cement composites, Kalderis et al. [59] reported that biochar addition promoted a 11.96 % flexural strength increase and a 22.2 % shrinkage reduction for the biochar-cement composites when compared to the reference group at 28 days. Qu et al. [60] using 2 wt% waste wood biochar to replace cement led to a 12.3 % water adsorption reduction and an increase of chemical chloride immobilisation when compared to biochar-free samples at 28 days. Thus, the self-healing capability of biochar-cement concrete requires to be further investigated and understood.

This study aims to analyse the self-healing behaviour of biochar-cement pastes incorporating CA, with three different curing conditions, including air curing, water immersion, and wet/dry cycle. Optical microscopy was used to monitor the time-dependent formation of the self-healing product up to 56 days. The interfacial-transitional zone (ITZ) between the self-healing product and the cementitious matrix was observed by Scanned Electron Microscopy equipped with Energy dispersive X-ray spectroscopy (SEM-EDS). Microstructural characterisation of the self-healing products was investigated using X-ray diffraction (XRD), Thermogravimetric analysis (TG), Fourier-transform Infrared Spectroscopy (FTIR), and Nuclear Magnetic Resonance (NMR). The novelty of this study is to investigate the self-healing performance of CA in biochar-cement composites, providing understandings of how biochar may influence the self-healing progress of cementitious composites.

2. Methodology

2.1. Raw materials and sample preparation

General purpose cement (GPC) traded by Boral Australia was used as the main binder. PENENTRON Admix CA (PENETRON, Australia) was utilised as the self-healing stimulator, and blended waste wood biochar (BWB) was obtained from Green Man Char (Australia) to partially replace GPC. The detailed information of CA and BWB, including chemical oxides, particle size distribution, and morphologies was reported in our previous study [42]. According to Lin et al. [42], the particle size distribution of BWB was ranged up to 200 μm with D10 D50, and D90 value of 2.31 μm, 10.54 μm, and 153.47 μm respectively. The mix designs for a paste prism (40 × 40 × 160 mm) are listed in Table 1. This study used a water-to-binder ratio of 0.35 for all groups. CO group refers to the reference group with 100 wt% GPC, and CC group refers to pastes with 1 wt% CA. CO group and CC group allows to investigate the impacts of CA only on the self-healing performance of CA-cement composites. In CB2 and CB5, the GPC is partially replaced by 2 wt% and 5 wt% BWB respectively, aiming to investigate the potential effects of biochar dosage in the self-healing process. It should be noted that BWB is used to partially replace GPC, while CA is used as an addition.

Firstly, all solid constituents were added and mixed in a 10 L Hobar Mixer with low-speed operation (16 rpm) for 2 mins to obtain a uniformly distributed powder mixture. Then, medium-speed mixing (24 rpm) was applied after adding ½ water content to the powder mixture for 3 minutes. Another 3-min mixing was performed after adding the rest of the water into the fresh mixture. It should be noted that the fresh cementitious mixture on the bowl of the mixer was then shovelled down followed by a 1-min mixing to avoid any loss of binder content. It is worth noting that superplasticiser (Sikament® Eco W*R*, Sika Australia) was used to achieved comparable flow results for samples with and without BWB (Table 1). After pouring the fresh mixture into the standard moulds (40 × 40 × 160 mm), all moulds were vibrated by 3 mins for a uniform mixture compaction. In total, 72 prisms were casted as illustrated in Table 2. Plastic foil sheet was used to cover all fresh pastes till the 24-hour demoulding. All hardened samples were placed in a conditioned humidity chamber with 23 ± 2 °C temperature and 95 ± 5 % relative humidity until testing.

2.2. Mechanical properties test

After demoulding, samples used for mechanical properties were cured in a water tank and tested at 7 days and 28 days. Complying with ASTM C348–21 [61], a AGX 50 universal testing machine was used to test the 7-day and 28-day flexural strengths of all samples. ASTM C349–18 [62] indicated that broken specimens following the flexural

Table 2
Sample casting details.

Experimental method	Mix design	Specimens	Condition
7-day and 28-day strengths	CO	6	Un-cracked
	CC	6	Un-cracked
	CB2	6	Un-cracked
	CB5	6	Un-cracked
Self-healing performance analysis	CO	6	Cracked
	CC	6	Cracked
	CB2	6	Cracked
	CB5	6	Cracked
Self-healing product collections	CO	6	Sliced
	CC	6	Sliced
	CB2	6	Sliced
	CB5	6	Sliced

Table 1
Pastes mix designs for self-healing behaviour analysis.

Mix designs	GPC	Water	CA	BWB	Superplasticiser	Water/binder ratio	Flow (mm)
CO	400 g	140 g	-	-	-	0.35	229 ± 1.6
CC	400 g	140 g	4 g	-	-	0.35	228 ± 0.7
CB2	392 g	140 g	4 g	8 g	2 g	0.35	227 ± 2.7
CB5	360 g	140 g	4 g	20 g	4.8 g	0.35	225 ± 1.9

Note: GPC means general purpose cement, CA refers to crystalline admixture, and BWB is blended waste wood biochar.

testings could be directly utilised to measure the compressive strength using an AGX 500 universal testing machine. In the study, the 7-day and 28-day compressive and flexural strength results were expressed by the average of three specimens.

2.3. Time-dependent self-healing monitoring

2.3.1. Crack initiation

After curing for a week in the controlled chamber, all samples were cracked by 3-point bending using an AGX 50 universal testing machine. Each sample was marked at 30 mm, 80 mm, and 130 mm from one end, and the centre position was obtained by aligning two marked lines on two roller supports as shown in Fig. 1a. Unlike several studies placed a steel bar in the middle of the specimen [17,63], a loading rate of 0.1 mm/min was directly applied to the marked specimens without steel bar (Fig. 1b). As given in Fig. 1c, the loading process was stopped after a crack initiated. It is worth noting that the prism did not break and remained unseparated.

2.3.2. Time-dependent monitoring

Cracked samples were cured in three conditions for 56 days, including direct air exposure curing (AR), permanent water immersion (WI), and wet/dry cycle after water curing (WD). For wet/dry cycle curing condition, cracked samples were exposed to water for 4 days and then dried in ambient condition of a controlled room for 3 days. It should be noted that all containers were stored in a controlled room with 23 ± 2 °C temperature and humidity of 50 ± 5 %. Two methods, including optical microscopy analysis and binary process were used to carry out a systematic investigation on the time-dependent formation of the self-healing products. In terms of optical microscopy, a Carl Zeiss Axiotech Vario 100 HD equipped with Jenoptik ProgRes CF Camera was used to observe the cracking line in all samples after cracks initiated (Fig. 2a). As shown in Fig. 2b, a typical optical microscopy image indicating the crack width was taken using a 10x-magnification lens in Zeiss microscopy. It should be noted that 5 lines were marked at 5 mm, 10 mm, 20 mm, 30 mm, and 35 mm from one end of the specimen to measure the crack widths at each location. The crack width for a specimen was the average result of 5 measurements.

For binary process analysis, images were taken for all samples after cracks initiated (Fig. 2c). In order to eliminate any image variance due to colour and brightness, a grey-scale regime was adopted (Fig. 2d). As illustrated in Fig. 2e, the background of each greyscale image was subtracted using ImageJ, while the cracking line was kept as the evidence of self-healing progress. In the third step, binary process function in ImageJ was utilised to convert greyscale cracking line into black-white image with a scale of 419 * 1343 pixels as shown in Fig. 3f, allowing the comparison of self-healing performance at different exposure time. Using ImageJ, the cracking line was represented by white pixels, while the reduction of total white pixels would be the evidence of a crack-closure process [64,65]. In this regard, a scale function in ImageJ was used to rescale all binary image to the same scale of 419 * 1343 pixels for area calculation. As shown in Fig. 2g, the cracking area of a CO sample (11,248 pixels) was calculate using ImageJ. Thus, the crack-closure rate (λ_{cr}) could be calculated based on Eq. 1:

$$\lambda_{cr} = \frac{A_t}{A_i} \times 100\% \quad (1)$$

Where λ_{cr} is the crack-closure rate (%), A_i is the initial cracking area, and A_t denotes the cracking area after exposure of t days.

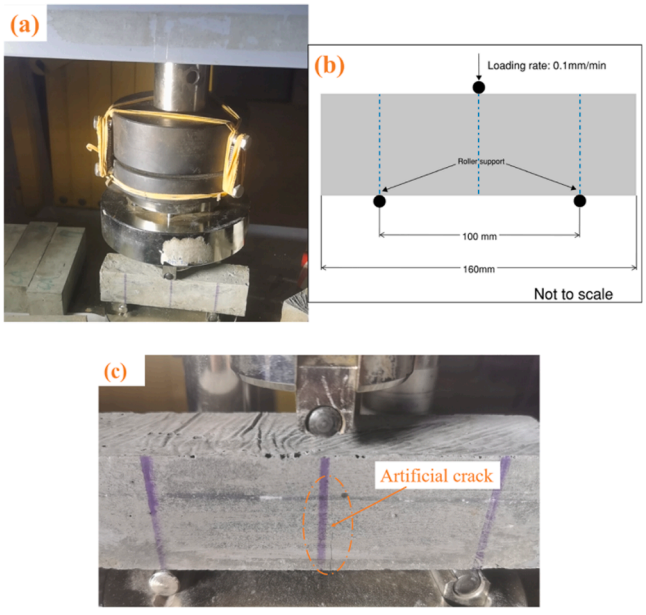

Fig. 1. Crack initiation: (a) 3-point bending set up; (b) Loading position and loading rate; (c) Cracked CO sample.

2.3.3. Scanned electron microscopy (SEM-EDS)

Zeiss Supra 55VP SEM equipment was utilised to analyse the self-healing product and interfacial transitional zone (ITZ) between cementitious matrix and the healed zone. As depicted in Fig. 3a, healed samples were coated with epoxy resin to avoid unexpected break due to strong vibrations during slicing process. Struers Labotom-15 cutting machine was used to cut sample along the cutting line (Fig. 3b). After that, a Struers Secotom-20 precise slicing equipment was employed to perform precise cut perpendicular to the healed crack (Fig. 3c). Sliced samples were then coated with iridium by a Leica EM ACE600 coater after drying in an oven at 45°C for 1 week (Fig. 3d). Furthermore, Energy dispersive X-ray spectroscopy (EDS) equipped in Zeiss Supra 55VP was used to identify the elemental compositions in self-healing products. The voltage was set at 10 kV and the working distance was set between 7 mm and 7.8 mm.

2.4. Self-healing product characterisations

As shown in Fig. 4, additional samples from each group (Table 2) were sliced into small portions with thickness of 10 mm. A rubber band was used to tie all portions during the exposure period (Fig. 4a). The adopted exposure condition was wet/dry cycle curing (WD) as mentioned in Section 2.3.2. At 56 days, each site was opened and washed using an isopropanol solution of 99.9 % purity. After that, the self-healing products were collected by carefully scratching each self-healing site (Fig. 4b). It should be noted that all powders were immersion in isopropanol for 2 days and dried in an oven at 45°C for 1 week after passing a 200 μm sieve. Finally, the self-healing product powders were analysed using X-Ray Diffraction (XRD), Thermogravimetric analysis (TG), Fourier-transform Infrared Spectroscopy (FTIR), and Nuclear Magnetic Resonance (NMR).

2.4.1. X-ray diffraction (XRD)

A Bruker D8 Discover diffractometer (Cu Kα, λ = 1.54 Å) was used to conduct the XRD analysis. The diffraction patterns of the self-healing products were measured at a step of 0.02° with the diffraction angle (2θ) range from 5° to 70° using a sample spinner. The mineralogical characterisations were obtained from Crystallography Open Database.

2.4.2. Thermogravimetric analysis (TG)

A NETZSCH STA 449 Jupiter was utilised to investigate the decomposition of self-healing products of the different group. Up to 30 mg powder of each healing products was added in an alumina crucible. The alumina crucible was then kept in a nitrogen environment at 40°C for 30-min standby. The heating process was set up to 1000°C with heating

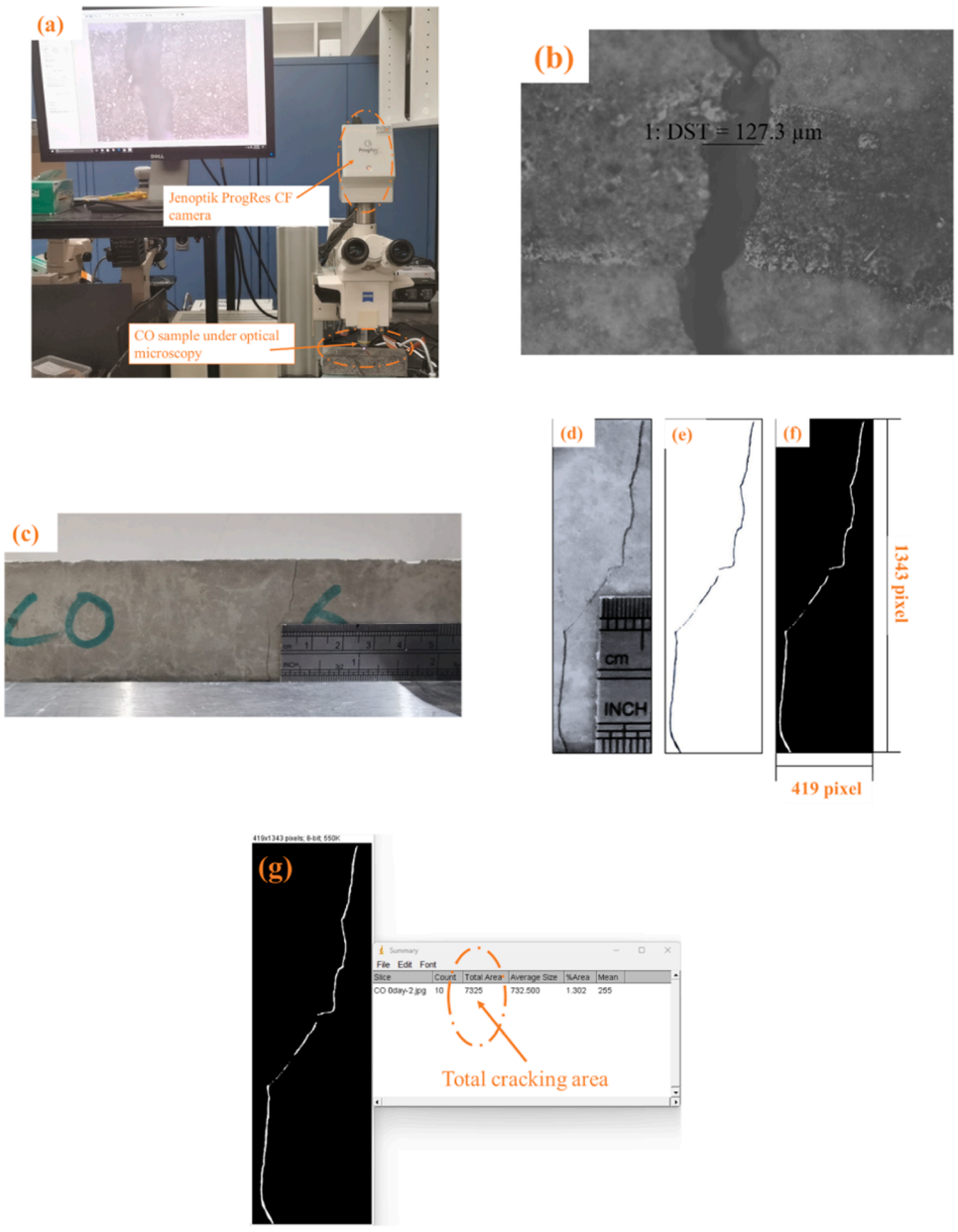

Fig. 2. Crack analysis of a cracked CO sample: (a) Optical microscopy observation set up; (b) Optical microscopy image with crack width; (c) original photo of cracked CO sample; (d) Crack observation in greyscale; (e) Crack observation with background-subtract process; (f) Crack observation with binary process; (g) Illustration of calculating cracking area.

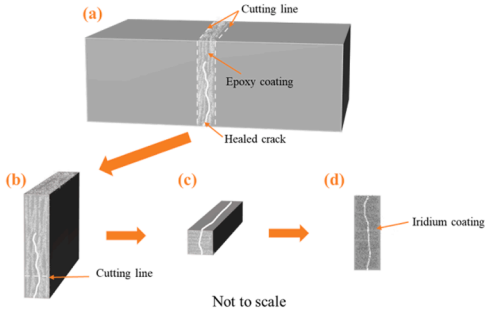

Fig. 3. Microstructural test sample preparation: (a) Epoxy resin coating; (b) Sliced portion with healed crack; (c) Precise cutting; (d) Sample with Iridium coating.

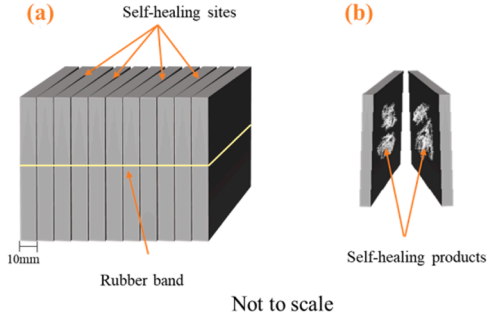

Fig. 4. Self-healing product preparation: (a) Sliced sample as self-healing sites; (b) Sliced portion for self-healing product scratching.

rate of 10°C/min and nitrogen gas flow rate of 50 ML/min [66,67]. Both TG and Derivative TG were recorded to analyse mass loss percentage of C-S-H gel, portlandite (CH), and calcite.

2.4.3. Fourier-transform infrared spectroscopy (FTIR)

FTIR analysis was conducted using a Nicolet 6700 FTIR spectrometer with a spectra ranging from 450 to 4000 cm^{-1} wavenumber. The resolution was set at 8 cm^{-1}.

2.4.4. Nuclear magnetic resonance (NMR)

The solid-state ^{29}Si spectra was obtained using an Agilent 500 MHz Nuclear Magnetic Resonance (NMR). Self-healing product powder was properly loaded in a 4-mm rotor, where the spinning rate was set at 12 kHz with 30 s relaxation delays. By using NMR, silicate anions (SO_4^{4-}) in the self-healing product were presented as the Q^1 to Q^4 peaks in the NMR spectrum [68,69]. Based on several studies [28,70], to determine Q^1 to Q^4 peaks, a deconvolution was conducted on the original ^{29}Si spectra using Gaussian model in the OriginPro 2021 software. The multipeak fit function was employed to calculate the area of each peak. Then the number of SiO_4 tetrahedra in C-S-H gel or polymerisation of C-S-H can be expressed using Eq. 2 [70–72],

$$\text{Mean chain Length(ML)} = \frac{2 \times (Q^1 + Q^2)}{Q^1} \quad (2)$$

3. Results

3.1. Mechanical properties

The mechanical properties of the different samples exposed to water immersion are compared in Fig. 5. In terms of compressive strength development, CA addition led to 8.89 % and 10.77 % improvement for 7-day and 28-day compressive strength in comparison to the CO group. This is attributed to a denser cementitious microstructure due to the CA addition, having a good agreement with previous studies [19,73]. 1 wt% CA and 2 wt% BWB in replacing cement promoted the highest compressive strength improvement at 7 days (16.60 %) and 28 days (16.62 %) when compared to CO group. Several studies [74,75] revealed that biochar released adsorbed water for additional curing improving hydration of the biochar-cement composites, leading to a higher compactness to resist compressive loads. However, although CA addition could improve the compressive strength, using 5 wt% BWB to replace cement interfered with the strength development with only 6.49 % and 8.25 % compressive strength increase at 7 days and 28 days respectively. Javed et al. [75] explained that the interference of strength development was due to the cement dilution, and higher amount of porous biochar leading to weak local ITZ to resist the loads.

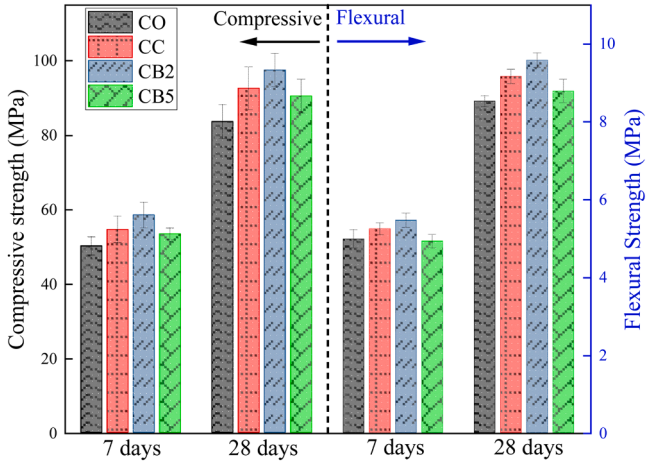

Fig. 5. Mechanical properties of cementitious samples exposed to water immersion.

For flexural strength, it could be noted that a lower strength increase was observed for all group (Fig. 5). At 7 days, the flexural strength improvement was 5.22 %, 9.67 %, and −1.21 % for CC, CB2, and CB5 respectively when compared to the control. Slightly higher strength improvement of 7.47 %, 12.39 %, and 3.07 % was found for CC, CB2, and CB5 respectively at 28 days.

Overall, the combination of 1 wt% CA and 2 wt% BWB in CB2 mix was the most effective option to improve the mechanical properties of biochar-cement composites, while higher dosage of BWB interfered with the strength development. However, CB5 mix still exhibited higher compressive and flexural strength than those of reference CO group at 28 days.

3.2. Time-dependent crack closure

Fig. 6 depicts the time-dependent healing process of all groups subjected to the three different exposure conditions, including AR (Fig. 6a), WI (Fig. 6b), and WD (Fig. 6C) using the optical microscopy. The exposure age was set at 0 day and 56 days. Notably, cracked samples cured in WD had the best healing performance, followed by samples cured in WI, and samples cured in AR demonstrated only limited self-healing capacity.

For AR exposure condition, the healing performance of all samples was very limited at 56 days (Fig. 6a). As shown in Fig. 6a5, no self-healing products were observed in the reference group. However, limited self-healing products were found in CC group (Fig. 6a6), CB2 group (Fig. 6a7), and CB5 group (Fig. 6a8). Similar findings were reported by other authors [17,76]. According to several studies [19,30], moisture was one of the main factors activating the special chemicals in CA improving the self-healing process. During AR curing period, cracked specimens were directly exposed to the ambient environment without any moisture supply. As a result, the self-healing behaviours of samples with CA was negligible.

For WI curing exposure, due to the presence of moisture around the cracked region, different self-repairing performance was observed for samples with and without CA addition (Fig. 6b). Partial crack repairing was observed in CC group (Fig. 6b6), CB2 group (Fig. 6b7), and CB5 group (Fig. 6b8), while no apparent healing products could be found in the reference CO group (Fig. 6b5) at 56 days. When compared to samples in AR exposure, more white deposits formed in the corresponding cracked region due to the water supply. Although larger cracking width (211.3 μm) appeared in CB5 group, self-healing product formed on both two sides of the crack and joined in the middle of the crack, partially sealing the cracks. Similar observations were found in CC and CB2 group with relatively thin cracking width (158 μm and 144 μm).

In terms of WD curing method (Fig. 6c), samples with CA demonstrated completed crack filling with white deposits at 56 days, being in a good agreement with other studies [38,77]. However, limited healing products were found in the crack surface at reference CO group (Fig. 6c5), which may be the products of continuous cement hydration. In this study, complete crack closure was observed between 150.7 μm (Fig. 6c6) and 205.3 μm (Fig. 6c8) with 1 wt% CA addition. By comparing the self-healing performance of the same mix subjected to WI and WD, samples cured in WD had superior healing efficiency than that of samples exposed to WI. Based on many studies [64,78,79], the white deposits could be classified as the mix of C-S-H gel, calcium hydroxide (CH), or calcium carbonate. Tittelboom et al. [80] interpreted that due to the availability of carbon dioxide, the self-healing efficiency was promoted. It was also evident in a study by Oliveira et al. [81], in which carbonated C-S-H and CH as the self-healing products was observed in Raman spectra. The characterisation of self-healing products is discussed in the following section.

Table 3 summarises the crack width closure of all samples exposed to wet/dry cycles up to 56 days. The average crack width was calculated based on 5 measurements. At 0 day, CB5 sample had the largest average

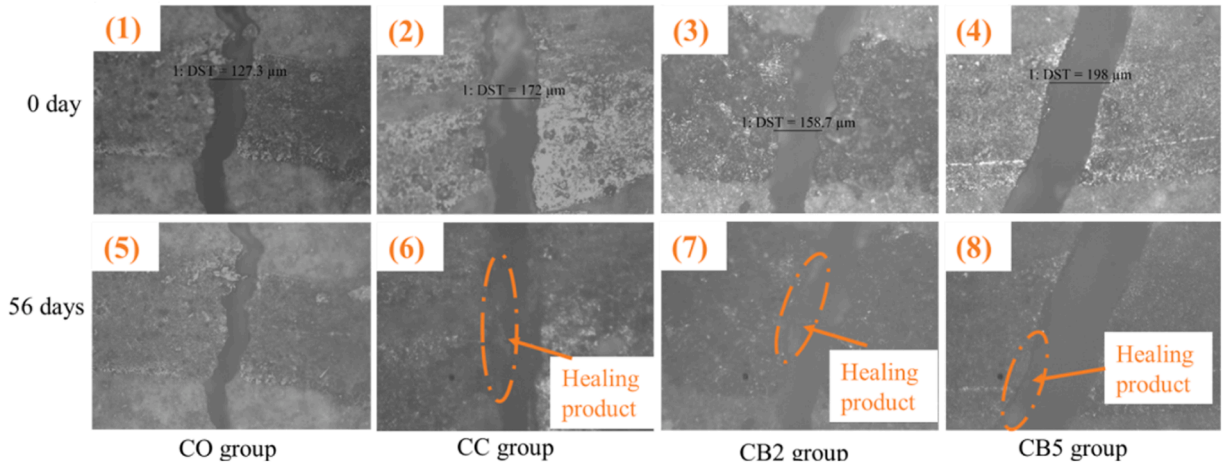

(a)

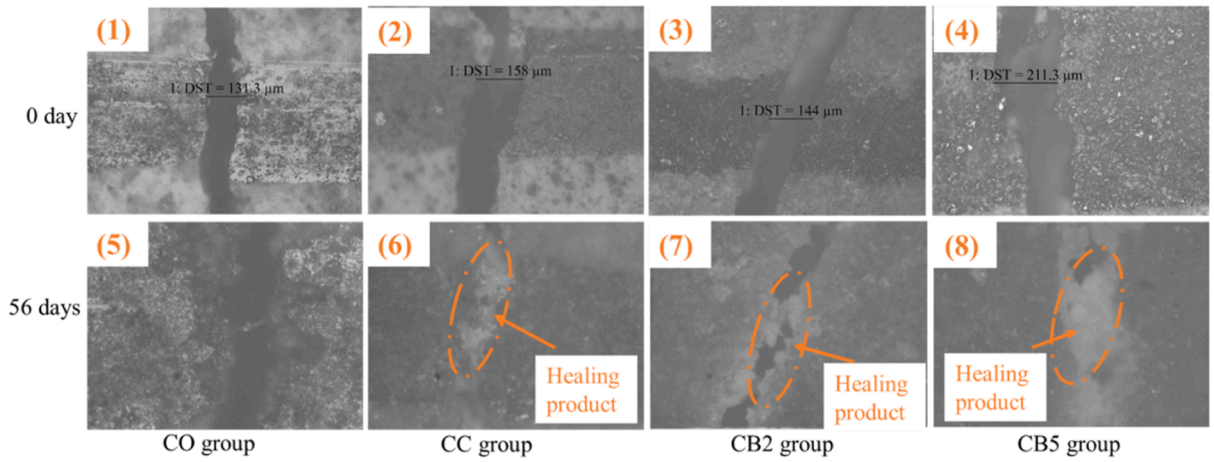

(b)

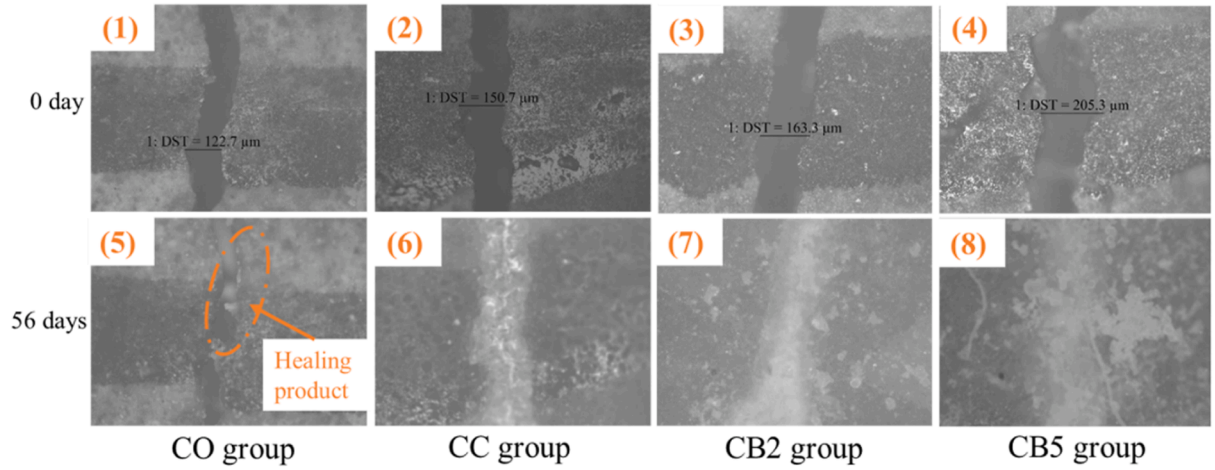

(c)

Fig. 6. Optical microscopy observations for samples cured in different conditions: (a) Air curing (AR); (b) water immersion (WI); (c) wet/dry cycle (WD). (Note: CO group is the reference group, CC group means samples with 1 wt% CA, CB2 group refers to samples with 1 wt% CA and 2 wt% BWB, and CB5 group donates samples with 1 wt% CA and 5 wt% BWB.

Table 3
Cracking width closure of all samples exposed to 8 wet/dry cycles.

Mix design	0-day		56-day	
	Average cracking width (μm)	Standard deviation (μm)	Average cracking width (μm)	Standard deviation (μm)
CO	121.53	2.48	90.31	20.12
CC	148.46	3.21	0	0
CB2	157.64	3.46	0	0
CB5	204.52	3.04	0	0

crack width of 204.52 μm with a standard deviation of 3.04 μm, while CO sample had the lowest average crack width 121.53 μm with a standard deviation of 2.48 μm. Complete crack closure was achieved in CC, CB2, and CB5 samples at 56 days, leading to the average crack width of 0 μm. However, due to absence of CA powder, only limited healing behaviour was found in the reference group reducing the average crack width to 90.31 μm with a standard deviation of 20.12 μm. It is worth noting that since healing products randomly formed on either side of the cracking surface of CO group (Fig. 6c5), significant differences in crack healing of CO group along the crack led to a relatively large standard deviation of 20.12 μm. Furthermore, the analyses of the time-dependent crack closure rate were carried out using binary image process in the following section.

Overall, WD seems to be the best exposure condition to promote the crack closure. With continuous supply of moisture, samples cured in WI had partial crack closure, and samples cured in WD demonstrated complete crack healing due to the presence of carbon dioxide.

3.3. Self-healing efficiency

To further quantify the self-healing efficiency of cracked samples exposed to WD, time-dependent cracking area was processed with binary images using ImageJ (Fig. 7). It should be noted that since the cracking line of CB2 group passed through a relatively large air bubble (Fig. 7c1), the air bubble was not included in the binary image (Fig. 7c3, Fig. 7c6, and Fig. 7c9), eliminating the negative effect on the cracking area analysis. Similar process was applied to the binary image of a CC group at 56 days (Fig. 7b9), where 3 small air bubble were removed. The time-dependent crack closure results are summarised in Table 4.

Fig. 8 presents the crack closure rate for all groups exposed to WD up to 56 days at the same scale of 419 * 1343 pixels. CB5 had the largest cracking area being 8608 pixels, biochar-free samples had cracking area of 7325 pixels and 7224 pixels for CO and CC group respectively. 5 wt% BWB replacing cement contributes to relatively more ductile BWB-cement matrix than the ordinary CO group, leading to a more tortuous cracking path (Fig. 7d1). Lin et al. [51] explained that the presence of biochar adsorbed cracking energy due to the weak ITZ between biochar and the cementitious matrix, interfering with the simple and flat cracking path development (Fig. 7a1 and Fig. 7b1). However, as shown in Figs. 5, 2 wt% BWB addition led to the highest flexural strength improvement, only having a cracking area of 6312 pixels.

At 28 days (4 wet/dry cycle), partial crack closure was observed for all groups. By comparing Fig. 7a1 and Fig. 7a4, due to the relatively narrow cracking width, the crack width in the middle of the cracked CO specimen was reduced with crack closure percentage of 17.91 %. This fact is attributed to the continuous hydration of the cementitious composites [82,83]. For CA-cement composites, significant crack closure percentage of 58.68 %, 55.39 % and 61.63 % was found for CC, CB2, and CB5 respectively. Notably, although CB5 sample had the highest initial cracking area of 8608 pixels, the lowest remaining cracking area was found in CB5 group (61.63 % cracking closure). It was evident in Fig. 7d4 that many white deposits were observed on the surface of the tortuous cracking path, indicating the effective self-healing process at 28 days.

At 56 days, clear white deposits were found in the cracking surface of all CA-cement composites indicating effective self-healing capacity of CA addition, being consistent with other studies [22,26,63,81]. Complete crack repairing was observed for CC and CB5 samples (Fig. 7b9 and Fig. 7d9). Due to the presence of a large air bubble in the middle of CB2 specimen, the crack closure was negatively impacted, being 97.38 %. However, it can be assumed that 100 % healing efficiency would be achieved in CB2 with the absence of air bubble. Thus, this study considered that there was complete crack closure in CB2 at 56 days. In terms of cracking closure rate, crack closure rate was slightly reduced for CA-cement composites (Fig. 8). Many studies [30,84,85] explained that special chemicals in CA stimulated the formation of calcium-based deposits using calcium ions in the cementitious matrix filling the crack. The formation of white deposits on the crack surface seems to interfere with the calcium ion leaching process, reducing the cracking healing rate from the fifth to the eighth wet/dry cycle in comparison with the first four cycles. Similar observation was reported by [3,33,38].

Overall, CA addition benefited the healing performance of the cementitious pastes. Using BWB to partially replace cement did not negatively affect the healing behaviour of the biochar-cement composites. In particular, due to a ductility improvement, CB5 had largest cracking area with complex and tortuous cracking path (Fig. 6), being completely healed at 56 days.

3.4. SEM-EDS analysis

Fig. 9 shows the preparation steps of a healed CC portion for ITZ analysis using SEM-EDS. It is worth noting that iridium was used to coat all healed portion, which would be marked in the EDS spectra.

Fig. 10a presents a SEM image of healing products in the cracking line with 100x magnification. It was found that the healing products had different morphological appearances. As shown in Fig. 10b, ball-shape self-healing products were observed with different sizes. Similar finding was reported in a study by Zhang et al. [3]. EDS mapping results confirmed the formation of calcite and carbonated C-S-H gels in the self-healing products (Fig. 10e and Fig. 10i), having a good agreement with many studies [3,86,87]. As depicted in Fig. 10i, C-S-H gel could be found in the bottom left of the zoom-in self-healing product A (Fig. 10b), and the healing product in the middle was mainly calcite. Likewise, Ferrara et al. [37] reported needle-like healing product on the crack surface after freeze/thaw cycle exposure. However, unlike ball-shape self-healing products formed in location A, rope-shape self-healing products were found in location B (Fig. 10c), indicating the morphological diversity of healing products. The EDS results of the point scan in Fig. 10f confirmed the formation of carbonated C-S-H gel filling the crack. Furthermore, calcite formation was found in point 2 at location B (Fig. 10g) and point 3 at location C (Fig. 10h).

It should be noted that a different density healing products were observed at various locations. Based on Fig. 10d, looser matrix was found in the surface of the healing product at location C (Fig. 10d), while denser matrix was observed in the healing product at location A (Fig. 10b). Meanwhile, at location B, loose and dense healing products were randomly formed, where dense healing product was surrounded by loose healing product (Fig. 10c).

Fig. 11 shows healing products in the CB5 sample after 4 wet/dry cycles (56 days). Based on EDS mapping at location D (Fig. 11d and Fig. 11h), calcite and carbonated C-S-H gels were found, being consistent with other studies [20,88]. Unlike limited C-S-H gel in reported healing products at location A in CC sample (Fig. 10i), higher portion of C-S-H gel was observed at location D in CB5 samples (Fig. 11h), distributed in the middle of location D. Fig. 11c illustrates a BWB particle formed with healing products in the ITZ of the CB5 sample. Similarly, biochar was found in the cracking path of the cracked biochar-cement composite after a fracture test [89]. Restuccia et al. [89] pointed that porous biochar tended to adsorb energy prior to the cementitious matrix due to weak load-bearing capacity.

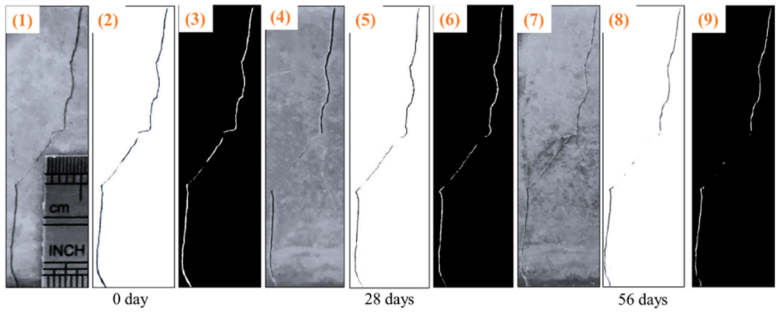

(a)

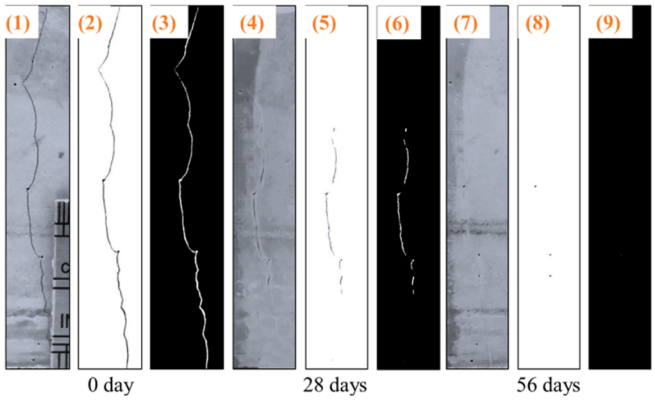

(b)

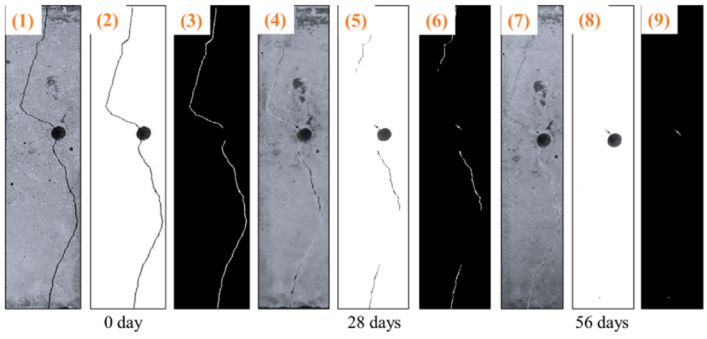

(c)

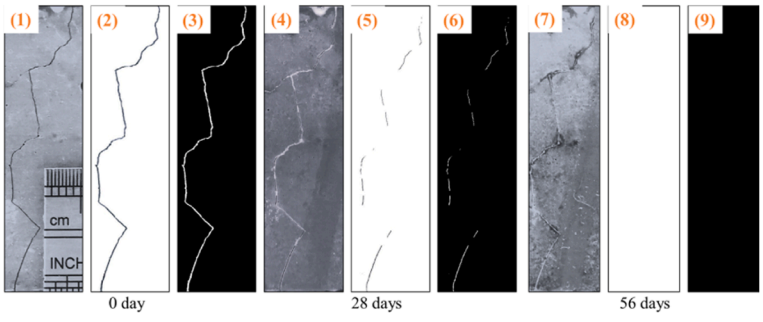

(d)

Fig. 7. Binary process: (a) CO group; (b) CC group; (c) CB2 group; (d) CB5 group. (Note: CO group is the reference group, CC group means samples with 1 wt% CA, CB2 group refers to samples with 1 wt% CA and 2 wt% BWB, and CB5 group donates samples with 1 wt% CA and 5 wt% BWB.

Table 4
Time-dependent crack closure of all samples in wet/dry cycle curing.

Mix design	Exposure age	Total image area (pixels)	Remaining crack area (pixels)	Healing percentage (%)
CO	0 day	562717	7325	0.00
	28 days	562717	6013	17.91
	56 days	562717	4513	38.39
CC	0 day	562717	7224	0.00
	28 days	562717	2985	58.68
	56 days	562717	0	100.00
CB2	0 day	562717	6312	0.00
	28 days	562717	2816	55.39
	56 days	562717	153	97.58
CB5	0 day	562717	8608	0.00
	28 days	562717	3303	61.63
	56 days	562717	0	100.00

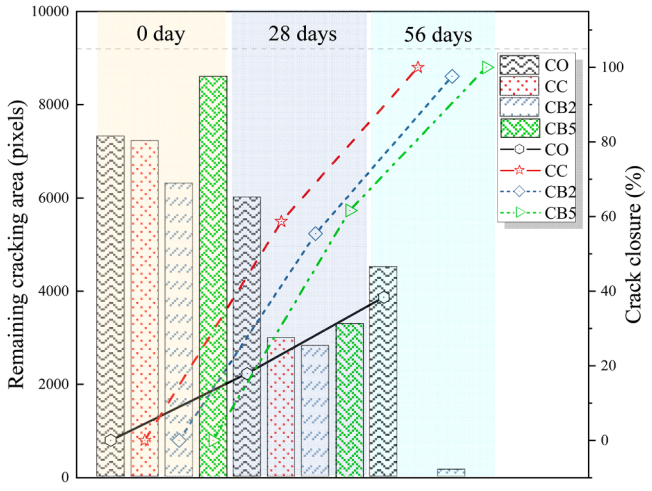

Fig. 8. Time-dependent crack closure of all specimens in WD curing.

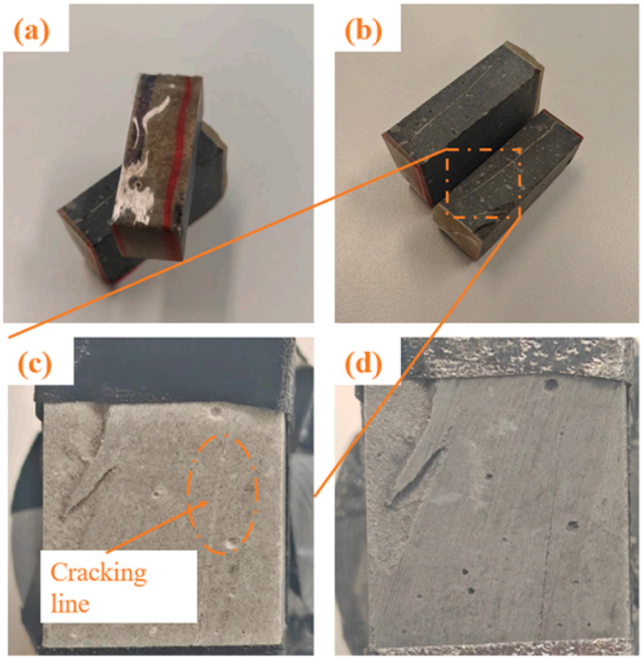

Fig. 9. SEM sample preparation of a healed CC sample at 56 days: (a) sample sliced from cementitious prism; (b) portion after precise cut; (c) Dried CC sample; (d) CC sample coated with Ir.

It could be found that BWB's pores provided additional sites for healing process. The EDS result of point scan revealed the formation of calcite inside BWB pores (Fig. 11f), while some calcite formed on the surface of BWB pore and adjacent healing product (Fig. 11e and Fig. 11g). Overall, by SEM-EDS analysis, similar healing products were observed in CC and CB5 samples along the cracking path, being mainly calcium-based deposits including calcite and small portion of carbonated C-S-H gel.

3.5. XRD analysis

The XRD patterns of self-healing products in CC, CB2, and CB5 group are shown in Fig. 12. Although XRD test was set to run up to 70° 2θ, the majority of peaks were located in the range of 10° 2θ to 60° 2θ. Thus, XRD results of three healing products were presented between 10° 2θ and 60° 2θ to investigate the formations of different mineral phases, including brucite, calcite, C-S-H, and portlandite.

The diffraction peak at 29.33° 2θ was classified as calcite, similar finding was reported by other studies [33,67,90]. Meanwhile, the diffraction of calcite was also observed at peaks of 23.01°, 35.88°, 39.3°, 43.1°, and 48.4° 2θ. Several studies [55,91] also observed similar peaks of calcite. The diffraction results of calcite were consistent with the SEM-EDS analysis at Section 3.4, where calcite was interpreted as the main healing products for all groups. Notably, CB2 group had the highest peaks of calcite compared to other two groups, indicating higher proportion of calcite forming in the cracks.

According to a study by Zhan et al. [67], diffraction peaks at 2θ of 32.5° and 49.3° were identified as C-S-H. However, low peaks of C-S-H were observed in the diffraction spectra (Fig. 12). One interpretation would be that limited amount of C-S-H formed during the healing process or part of the C-S-H has been carbonated, leading to low C-S-H peaks. Another C-S-H peak was located at 2θ of 26.5°, being consistent with a study by Li et al. [90]. Other mineral phases of brucite and portlandite were observed at 2θ of 18.1°. Additional portlandite peaks were found at 2θ peak of 27.5°, 34.1°, 46.9°, and 47.4°. Similar portlandite peak was observed at 27.2° [90] and 47.14° 2θ [55].

Overall, XRD results revealed that the main healing products were calcite, while small portions of C-S-H gel and portlandite was identified, which is consistent with SEM-EDS results in Section 3.4.

3.6. TG/DTG analysis

TG/DTG analysis was carried out to quantify the formation of different mineral phases in the healing products for all groups subjected to 4 wet/dry cycles at 56 days. The first peak at DTG curve is the dehydration of C-S-H and ettringite in the temperature range of 60–250 °C [3,50,91]. However, due to difficulty in separating the mass loss of C-S-H and ettringite at the first DTG peak [3], this study would donate this mass loss percentage in the temperature range of 60–250 °C as δ_{other} for all groups. DTG peaks at temperatures of 400–500 °C and 600–800 °C are identified as decomposition of portlandite [66,91] and decarbonation of calcite respectively [16,50,92].

As depicted in Fig. 13, significant peak was observed in the temperature range of 600–800 °C in the DTG curve, indicating calcite being the main healing product for all groups. Relatively small peaks were marked for decompositions of C-S-H gel (60–250 °C) and portlandite (400–500 °C). It should be noted that the blue line representing CB2 group in Fig. 13 had the highest endothermic peak of calcite and lowest peak of C-S-H gel. However, CC and CB5 had three similar endothermal peaks. It should be noted that by focusing on the mass loss of calcite in DTG curve (Fig. 13), the temperature reaching endothermal peak varied, being 753.59 °C, 756.69 °C, and 763.62°C for CC, CB2, and CB5 respectively. The mass percentage of portlandite and calcite were calculated as δ_{CH}% (portlandite) and δ_C% (calcite) using Eq. 3 and Eq. 4 respectively.

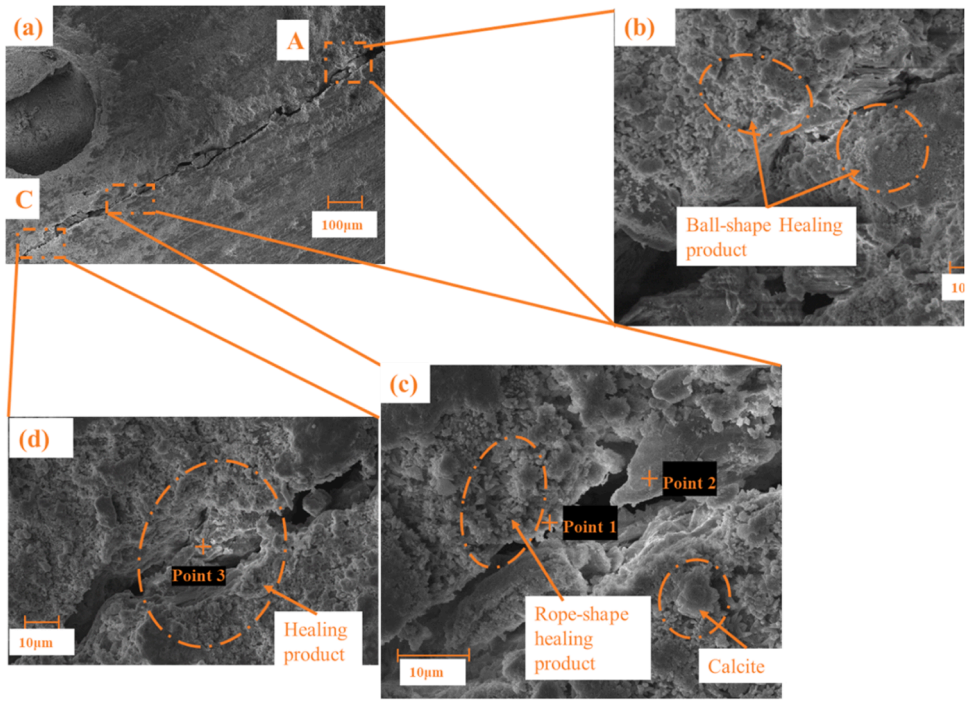

Fig. 10. Healed CC sample at 56 days: (a) Healing products ITZ at CC sample: (b) Self-healing product at location A; (c) Self-healing product at location B; (d) Self-healing product at location C; (e) EDS mapping result of self-healing product at A; (f) EDS result of point scan at point 1; (g) EDS result of point scan at point 2; (h) EDS result of point scan at point 3; (i) Elemental distribution of EDS Mapping at A.

$$\delta_{CH}\% = (M_{400} - M_{500}) \times \frac{78}{18} \quad (3)$$

$$\delta_{C}\% = (M_{600} - M_{800}) \times \frac{100}{44} \quad (4)$$

where M_{400}, M_{500}, M_{600}, and M_{800} are the mass loss percentages in TG curve respectively. 78, 18, 100, and 44 are the molar mass of portlandite, water, calcite, and carbon dioxide respectively.

Fig. 14 shows the quantitative analysis of the TG results in percentage. The major mineral phase was calcite for all groups, being 50.79 %, 64.25 %, and 53.44 % for CC, CB2, and CB5 respectively, having a good agreement with XRD results in Fig. 12. Similar calcite content in self-healing products were reported by Xue et al. (59.5 %) [33], while only 40 % calcite was found in healing products based on fly ash-cement composites [3]. By comparing the mass percentage of calcite, the presence of BWB seemed to promote the formation of calcite during the self-healing process. It was evident from Fig. 11e and Fig. 11f, where BWB provides additional sites for self-healing formations. It was found that three groups had similar portlandite contents, being 9.50 %, 9.42 %, and 9.69 % respectively. Since samples cured in WD condition were exposed to carbon dioxide during the drying cycles, the formation of portlandite would be carbonated to form calcite. However, it was complicated to quantitatively analyse the mass percentage of CSH in healing products using TG/DTG results [34,87]. Thus, this study did not compare the mass loss during the thermal event at temperature ranging from 60 to 250 °C, donated as δ_{other}. However, by combining XRD diffraction patterns (Fig. 12) and TG/DTG results (Fig. 13), formation of small portion CSH was confirmed.

3.7. FTIR

The FTIR spectra of different self-healing products was presented in Fig. 15. Obvious peaks at 711 cm^{-1}, 872 cm^{-1} and 1407 cm^{-1} were classified as bands for C-O representing carbonated ion [93,94], indicating the formation of calcite in the healing products. It could be noted that the blue line (CB2 group) had the highest peak of C-O bands, agreeing with XRD and TG results. Based on several studies [33,95], due to the carbonation or the aluminium content of CSH gel, the signals of Si-O varied from 970 cm^{-1} to 998 cm^{-1}. For the next peak in the spectra at 964 cm^{-1} to 989 cm^{-1}, Si-O bands was observed. Furthermore, the variances of signal intensity of Si-O bands at different spectra curves confirmed the presence of both carbonated C-S-H and C-S-H gels in the healing products. The band peaks at 1652 cm^{-1}, 3649 cm^{-1} and 3743 cm^{-1} were marked as H-O [93,96], revealing the presence of portlandite in the healing products.

3.8. ^{29}Si NMR

Based on several studies, Q^0, Q^1, Q^2, Q^3, and Q^4 could be identified in the chemical shift at −73, −81, −87, −93 to −96, and −103 to −106 respectively [28,97,98]. Q^1 value mainly means the SiO_4^{4-} group at an end of C-S-H chain, where Q^2 value indicates the SiO_4^{4-} group in the middle of C-S-H chain. Q^1 and Q^2 are used to establish the silicate polymerisation via ML [72]. In terms of Q^3, it refers to the SiO_4^{4-} group attached on the C-S-H chain in sheet shape, and Q^4 is the SiO_4^{4-} group attached on the C-S-H chain with two end to form framework shape [98,99]. Higher portion of Q^3 and Q^4 could suggest denser C-S-H gel. The deconvolution results of ^{29}Si NMR are depicted in Fig. 16 using a multipeak fit function in OriginPro.

Since NMR results mainly reveals the structure and polymerisation of CSH gels [100,101], the NMR spectra does not reflect the formation of portlandite and calcite (Fig. 16). It could be used to further analyse the formation of different C-S-H gels in the healing products. The area integral results are summarised in Table 5. As shown in Fig. 16d, CB2 group had the highest Q^1 (16.57 %) and Q^2 (63.42 %) value when compared to CC and CB5. In other words, the C-S-H gel formed in CB2 group had more SiO_4^{4-} groups attached on the C-S-H chain, indicating high degree of polymerisation. Similar findings were reported by other studies [72,98]. Based on Eq. 2, the mean chain length (ML) was

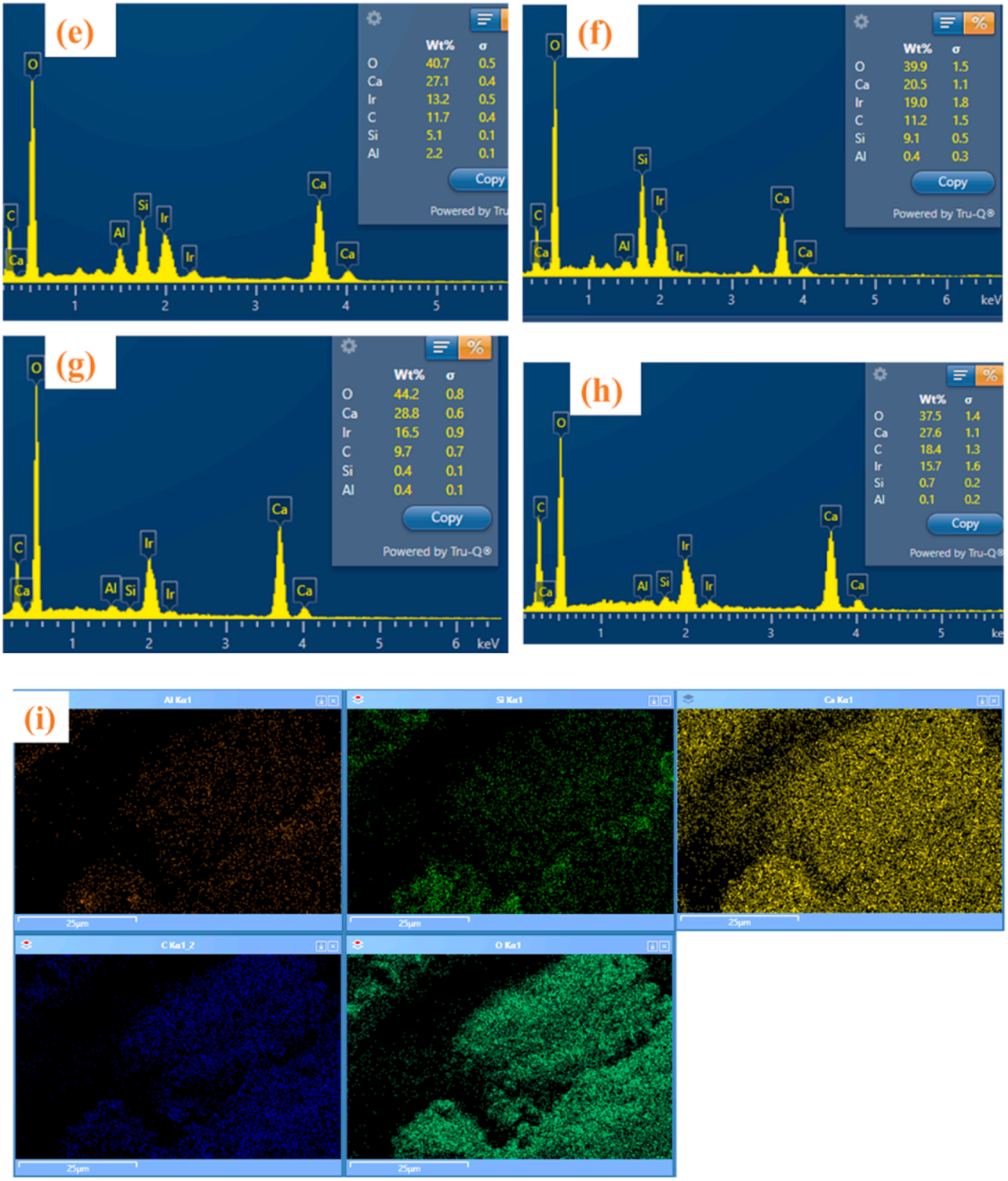

Fig. 10. (*continued*).

calculated using Q^1 and Q^2 (Table 4). It could be noted that ML (12.15) of CB2 was significantly higher than that of CC and CB5, being 5.05 and 4.7 respectively. However, XRD and TG/DTG results in this study revealed that lower portion of C-S-H gel was found in CB2 when compared to CC and CB5 group, which might lead to significant differences in ML. As a result, C-S-H gel in CB2 group seemed to have higher polymerisation level based on ML calculation.

For Q^3 and Q^4, CC group (34.63 %) had similar Q^3 with CB5 group (37.13), being higher than that of CB2 group (12.5 %), while the Q^4 values were 10.09 %, 3.64 %, and 6.47 % for CC, CB2, and CB5 respectively. Since Q^3 indicates sheet-shape SiO_4^{4-} group and Q^4 is framework-shape SiO_4^{4-} group, higher Q^3 and Q^4 supports a denser C-S-H gel. Thus, in CC and CB5 group, healing products might have denser C-S-H gel than that of CB2 group.

Overall, since limited amounts of C-S-H gels were observed in XRD and TG results, the NMR could only provide a reference comparison on the structure and polymerisation of formed C-S-H gel in the healing

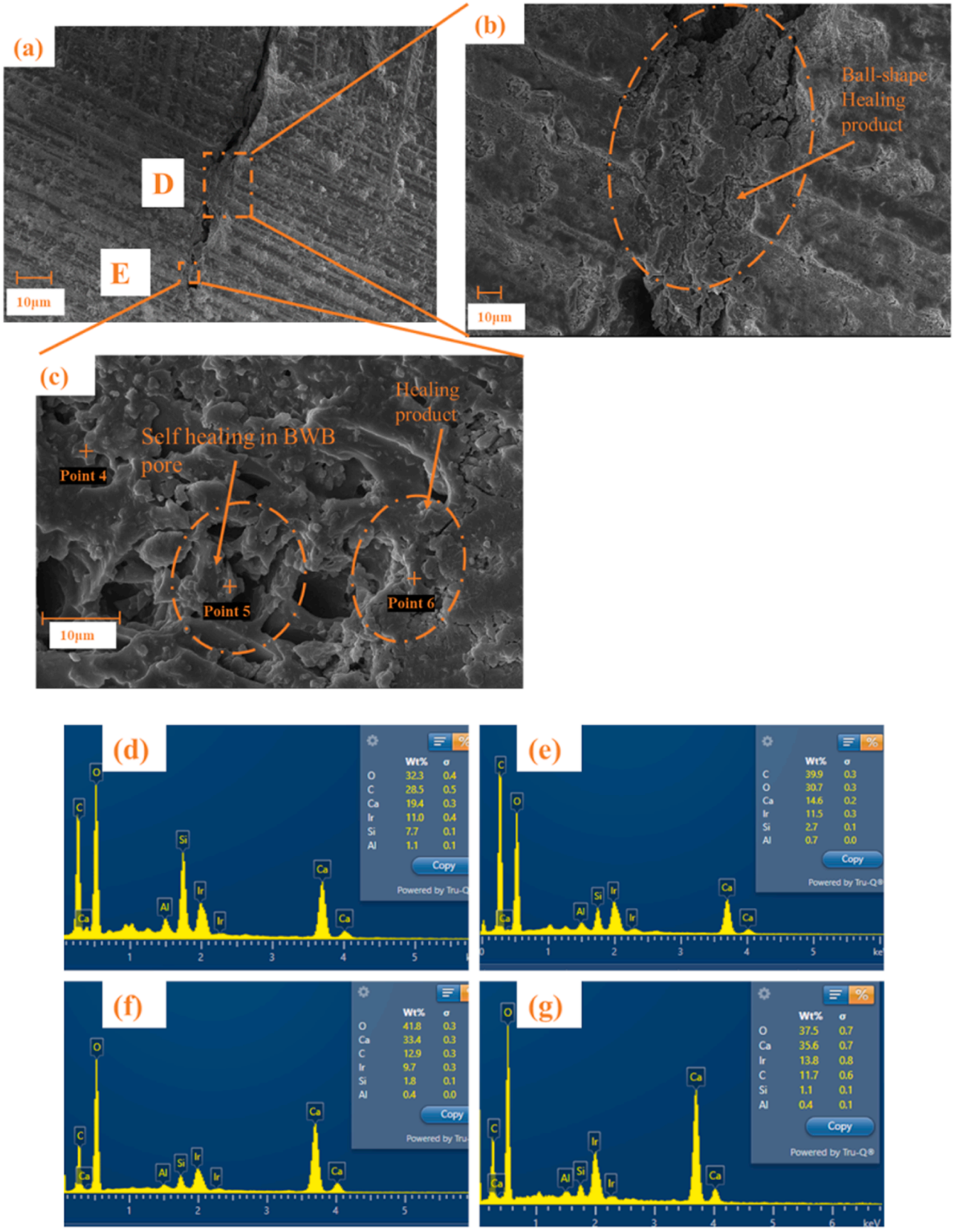

Fig. 11. Healed CB5 sample at 56 days: (a) Healing product ITZ at CB5 sample; (b) Healing product at location D; (c) Healing product at location E; (d) EDS mapping result of self-healing product at D; (e) EDS result of point scan at point 4; (f) EDS result of point scan at point 5; (g) EDS result of point scan at point 6; (h) Elemental distribution of EDS mapping at D.

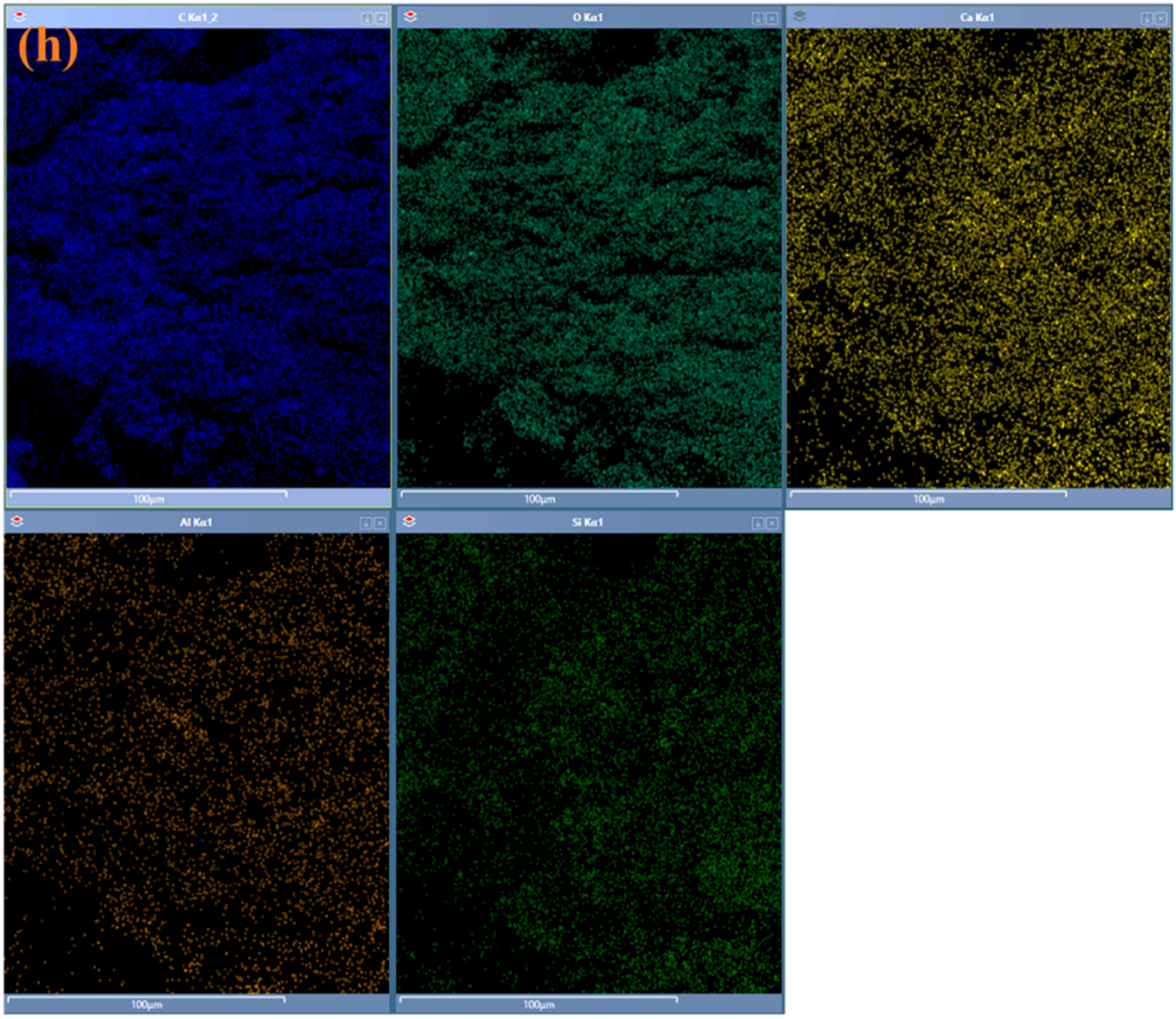

Fig. 11. (*continued*).

products. Nevertheless, NMR results suggested that C-S-H gels in the healing products of CB2 had higher level of polymerisation, while C-S-H gels in healing products of CC and CB5 had denser chain structures.

4. Discussions

4.1. Effects of CA on self-healing process

The self-healing process of CC sample is depicted in Fig. 17. At 0 day, the initial crack width was 150.7 μm. The CA and capillary pores are randomly distributed in the cementitious matrix (Fig. 17a). It should be noted that although CA could promote a denser cementitious matrix, the brittle nature remained the same, leading a flat and straight cracking path (Fig. 7b1).

At 28 days, based on Fig. 7b4, the initial crack was partially sealed up to 58.68 % by white deposits (Fig. 8). Meanwhile, due to the moisture supply during the WD cycle, capillary pores were partially or completed filled by crystalline deposits. Although only narrow cracks were healed at 28 days, in general, self-healing products initially formed on both site of the crack surfaces, propagating toward the middle of the crack (Fig. 7b4). Furthermore, the cracking line in CC group was completely healed by white deposits at 56 days (Fig. 17c), being evident from Fig. 6c6 and 7b7. EDS mapping confirmed the formation of calcium-based crystalline deposits in the cracking region (Fig. 10e and Fig. 10i). According to the elemental analysis in Fig. 10e, both calcite and carbonated C-S-H were identified. Meanwhile, self-healing products formed with different density and morphology were observed in the SEM-EDS analysis (Fig. 10b to Fig. 10d).

XRD results and TG/DTG curves confirmed that the main healing products were calcite, being 50.79 % in the mass loss calculation. Likewise, small portion of portlandite was observed based on XRD and TG results. FTIR and NMR spectra revealed the presence of C-S-H in the healing product of CC group. However, due to the difficulty in classify C-S-H at endothermic event up to 200 degrees in the TG analysis, the mass percentage of C-S-H gel was not reported.

Overall, CA addition significantly improves the healing efficiency of GPC paste, which is governed by several factors: CA has the ability to trigger the formation of crystalline deposits blocking voids and pores in the cementitious matrix, highlighting its favourable benefit in improving the compressive strength [102,103]. Then, the accumulation

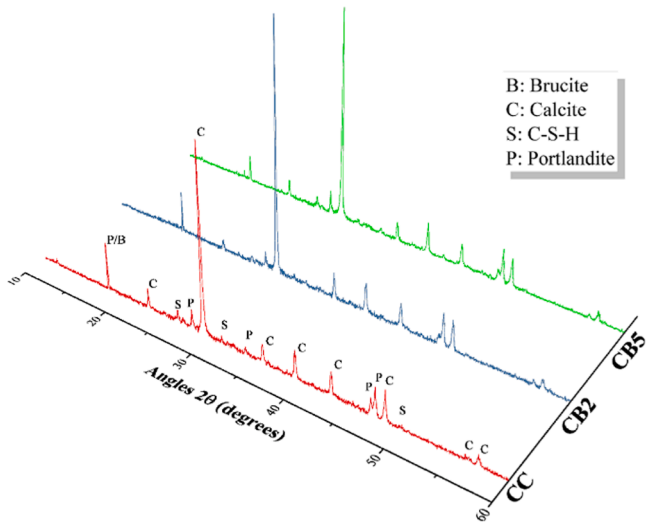

Fig. 12. XRD patterns of self-healing products.

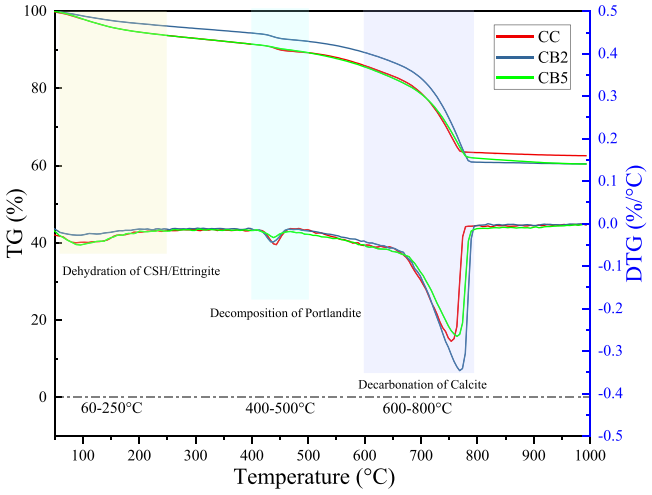

Fig. 13. TG/DTG analysis.

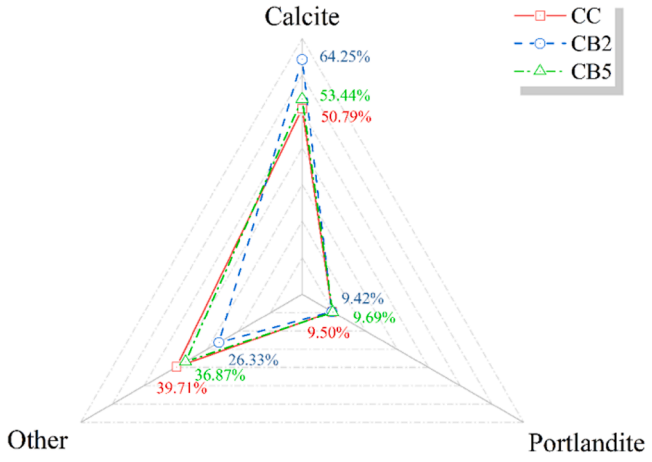

Fig. 14. Quantitative analysis of mineral phases.

of CA on the cracking region prolongs the healing behaviour [78,85,104,105]. In this study, the self-healing products repaired the crack (150.7 μm) at 56 days, indicating the long-term healing ability of CA.

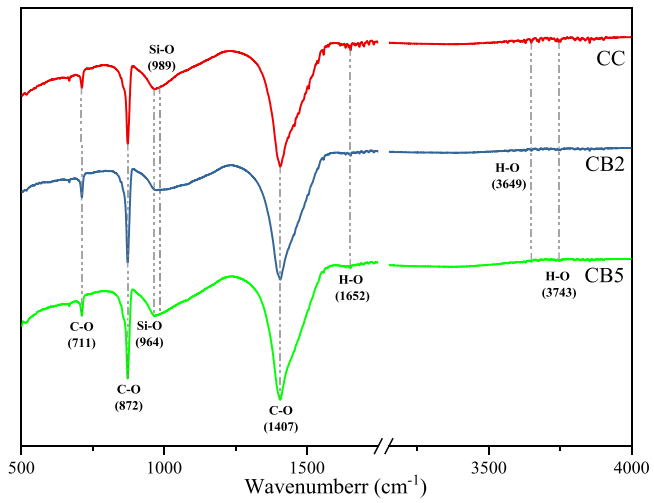

Fig. 15. FTIR spectra of healing products.

4.2. *Effects of BWB on self-healing process*

This study used porous BWB to partially replace cement up to 5 wt%, and the morphological characteristics were reported in our previous study [42]. The pores of BWB could provide additional sites for hydration as well as self-healing. The first benefit of BWB addition was the fracture energy adsorption, leading to a more tortuous cracking path when compared to other groups (Fig. 7c1 and Fig. 7d1). Meanwhile, by comparing the optical microscopy images (Fig. 6a4, Fig, 6b4, and Fig. 6c4), wider cracking widths were observed in CB5 sample (up to 211.3 μm).

Fig. 18 shows a schematic diagram of the self-healing process in a CB5 sample up to 56 days. A crack of 211.3 μm was observed using an optical microscope (Fig. 6c4). From Fig. 11c, BWB presented at the crack surface, indicating that cracking occurred through weak BWB particles. After 4 WD cycles, several healing products were found on the crack surfaces, due to stimulation of CA to produce crystalline deposits (Fig. 18b). It was evident in the binary analysis, where white deposits were found on the cracking surface (Fig. 7c4 and Fig. 7d4). Up to 55.39 % and 61.63 % crack closure was estimated from the binary analysis at 28 days (Fig. 8). As shown in Fig. 18b, self-healing products formed on each side of the crack reducing the cracking width. It should be noted that some portion of healing products formed on the BWB's surface and pores (Fig. 11c).

At 56 days, it was worth noting that the initial crack was completely repaired by white deposits (Fig. 7c7 and Fig. 7d7). By combining the EDS results in Fig. 11e and Fig. 11f, calcium-based products formed in BWB's pores and the surface of BWB, while the cracked side of BWB were bridged with healing products such as calcite (Fig. 11g). XRD results (Fig. 12) and TG/DTG results (Fig. 13) confirmed the formation of calcite, small portion of portlandite and C-S-H gels. From the mass loss difference, 53.44 % calcite and 64.25 % calcite were found in 30 mg self-healing products in CB5 and CB2 samples respectively. FTIR and NMR spectra confirmed the limited formation of C-S-H gels. However, XRD patterns and TG curve of CB2 group indicated only limited amount of C-S-H gels, where the carbonated C-S-H layer may interfere with the corresponding signal gathering. Although the widest crack width was found in CB5 group, it was completely healed at 56 days (Fig. 7d7 and Fig. 18c).

Overall, the superior healing capacity of biochar-cement composites with CA is governed by two aspects: firstly, the presence of biochar improves the fracture resistance by ductility improvement, where tortuous cracking path offer more nucleation sites for the self-healing process with formation of different crystalline deposits. Secondly, CA significantly promotes the healing efficiency of the biochar-cement

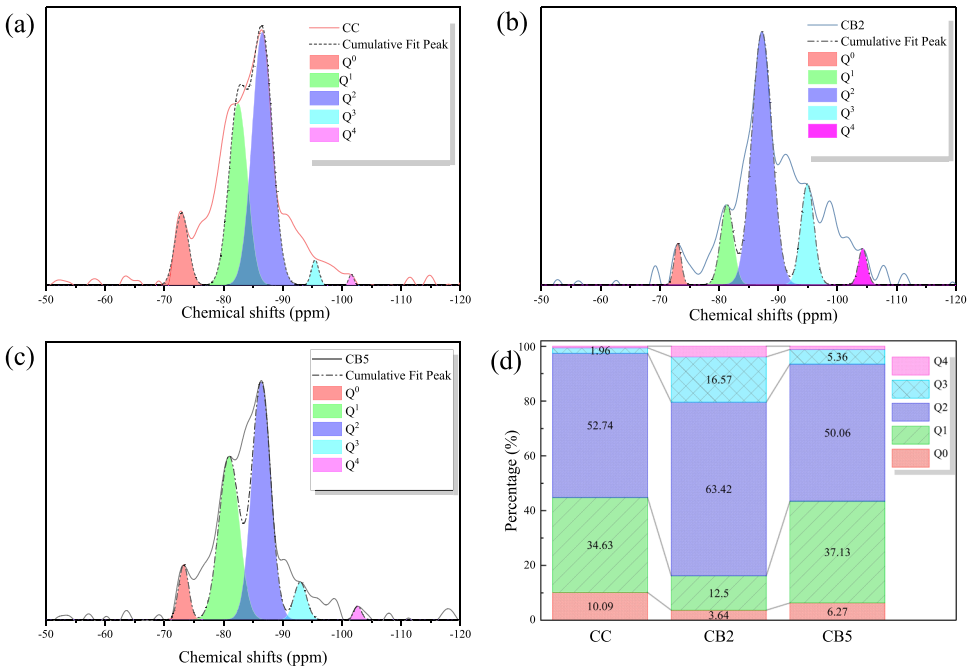

Fig. 16. 29Si NMR results: (a) CC group; (b) CB2 group; (c) CB5 group; (d) Comparison of Q values.

Table 5
Peak area integral in percentage.

Calculation target	Mix design		
	CC	CB2	CB5
0	10.09	3.64	6.27
1	34.63	12.50	37.13
2	52.74	63.42	50.06
3	1.96	16.57	5.36
4	0.58	3.87	1.19
ML	5.05	12.15	4.70

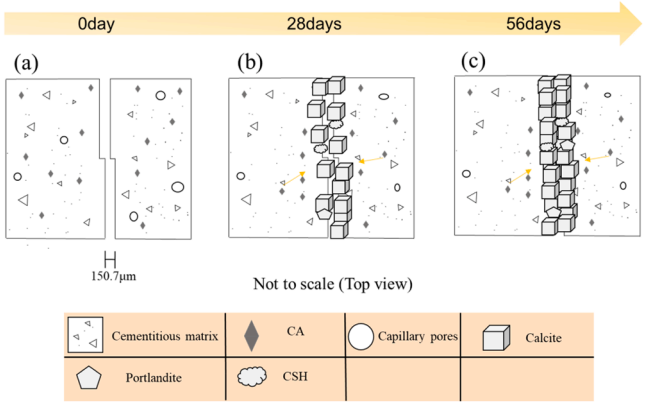

Fig. 17. Schematic diagram of self-healing process in a CC sample.

composites, in presence of water and carbon dioxide.

5. Conclusion

This study investigates the potential effects of CA and BWB on the self-healing behaviours of the General Purpose cement paste via artificial load-induced cracking using three-point bending. The self-healing efficiency was evaluated using both optical microscopy and binary analysis. The self-healing products were analysed using SEM-EDS, XRD,

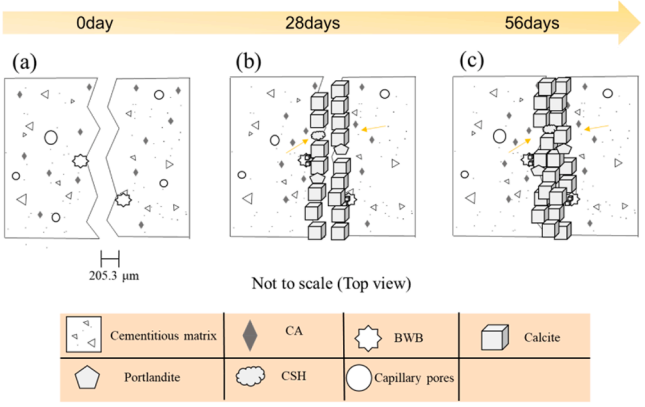

Fig. 18. Schematic diagram of self-healing process in CB5 sample.

TG, FTIR, and NMR. The main conclusions are as follows:

(1) Based on the optical microscopy and binary analysis, wet/dry cycle (WD) was the best exposure condition improving the self-healing efficiency, since crack was completed healed for samples with 1 wt% CA (CC) and samples with 1 wt% CA and various biochar content (CB2 and CB5) at 56 days.
(2) Using up to 5 wt% biochar did not negatively interfere with the mechanical strength development of CB5 group when compared to the reference group at 28 days. The combination of 1 wt% CA and 2 wt% BWB (CB2 group) demonstrated the best mechanical properties, promoting 16.62 % and 12.39 % strength increment for compressive and flexural strength respectively when compared to CO group at 28 days.
(3) In WD exposure condition, CB5 group achieved up to 61.6 % crack closure at 28 days. At 56 days, CO group achieved 38.39 % crack closure, while the other three groups reached 100 % crack healing.
(4) 5 wt% biochar (CB5) led to a more torturous cracking path. Biochar particle provided more nucleation sites for the self-

healing process, healing wider cracking width when compared to CA group.

(5) SEM-EDS results observed the formation of calcium-based crystalline deposits along the cracking line. XRD and TG results confirmed the formation of calcite and a small portion of portlandite in the healing products. CB2 had the highest calcite percentage of 64.23 % in 30 mg healing products, followed by 53.44 % and 50.79 % for CB5 and CC respectively.

(6) FITR and NMR spectra confirmed a limited formation of C-S-H gels in the healing products. Using deconvolution method, the values of Q^1 and Q^4 showed that C-S-H gels in healing products of CB2 had a higher level of polymerisation, while C-S-H gels in healing products of CC and CB5 had a denser chain structure. Similar self-healing products were observed in composites with and without the presence of waste wood biochar.

(7) Although a thorough investigation was conducted to understand the self-healing behaviour of biochar-cement composites incorporating CA, more studies are required to explore the self-healing performance of biochar-cement composites with CA subjected to aggressive environments, such as marine environment or freeze/thaw cycle.

CRediT authorship contribution statement

Quang Dieu Nguyen: Writing – review & editing, Supervision, Resources, Project administration, Investigation, Formal analysis, Conceptualization. **Xuqun Lin:** Writing – original draft, Visualization, Validation, Methodology, Investigation, Formal analysis, Data curation, Conceptualization. **Peiran Li:** Writing – review & editing, Investigation. **Arnaud Castel:** Writing – review & editing, Supervision, Resources, Project administration, Investigation. **Vivian W. Y. Tam:** Writing – review & editing, Investigation. **Wengui Li:** Writing – review & editing, Investigation.

Declaration of Competing Interest

The authors declare that they have no known competing financial interests or personal relationships that could have appeared to influence the work reported in this paper.

Acknowledgements

The authors highly appreciate Australian Research Council (DP220101051), Australia and the supports from University of Technology Sydney Research Academic Program at Tech Lab (UTS RAPT). The technical supports regarding solid-state NMR from Dr. Robin Wang at Faculty of Science, UTS were appreciated.

Data availability

Data will be made available on request.

References

[1] B. Mather, Concrete durability, Cem. Concr. Compos. 26 (1) (2004) 3–4.
[2] Y. Tian, G. Zhang, H. Ye, Q. Zeng, Z. Zhang, Z. Tian, X. Jin, N. Jin, Z. Chen, J. Wang, Corrosion of steel rebar in concrete induced by chloride ions under natural environments, Constr. Build. Mater. 369 (2023) 130504.
[3] C. Zhang, R. Lu, Y. Li, X. Guan, Effect of crystalline admixtures on mechanical, self-healing and transport properties of engineered cementitious composite, Cem. Concr. Compos. 124 (2021) 104256.
[4] M. Gharieb, S.A. Aboutaleb, A.M. Dokaila, M. El-Attar, Impact of combined organic chemical inhibitor on mechanical properties of cement pastes and steel reinforcement corrosion in concrete upon exposure to aggressive environment, Constr. Build. Mater. 420 (2024) 135567.
[5] D.J. De Souza, L.F.M. Sanchez, Understanding the efficiency of autogenous and autonomous self-healing of conventional concrete mixtures through mechanical and microscopical analysis, Cem. Concr. Res. 172 (2023) 107219.
[6] M. Cassidy, J. Waldie, S. Palanisamy, A method to estimate the cost of corrosion for Australian defence force aircraft. Proc., 16th Australian Int. Aerospace Congress., Engineers Australia, Melbourne, Australia. Barton, ACT, Australia, 2015.
[7] H. Tabatabai, M.D. Pritzl, A. Ghorbanpoor, Evaluation of select methods of corrosion prevention, corrosion control, and repair in reinforced concrete bridges, Wisconsin Highway Research Program, 2009.
[8] Y. Wang, Y. Miao, Y. Li, F. Wang, S. Mu, L. Wang, S. Gao, Z. Lu, Z. Liu, J. Jiang, Investigation of the damage self-healing and chloride-water coupled transport inhibition mechanism of microencapsulated concrete, Constr. Build. Mater. 435 (2024) 136838.
[9] J. Fronczyk, M. Janek, M. Szeląg, A. Pyzik, W. Franus, Immobilization of (bio-) healing agents for self-healing concrete technology: does it really ensure long-term performance? Compos. Part B: Eng. 266 (2023) 110997.
[10] X. Pan, B. Gencturk, Self-healing efficiency of concrete containing engineered aggregates, Cem. Concr. Compos. 142 (2023) 105175.
[11] Y. Shields, E. Tsangouri, C. Riordan, C. De Nardi, J.R.A. Godinho, T. Ooms, P. Antonaci, D. Palmer, A. Al-Tabbaa, T. Jefferson, N. De Belie, K. Van Tittelboom, Non-destructive evaluation of ductile-porous versus brittle 3D printed vascular networks in self-healing concrete, Cem. Concr. Compos. 145 (2024) 105333.
[12] J. Xu, X. Wang, W. Yao, Q. Chen, H. Zhu, S.P. Shah, Understanding the formation and structure of bio-mineralization for self-healing of marine concrete: an experimental and thermodynamic approach, Cem. Concr. Compos. 145 (2024) 105369.
[13] Y. Fang, H. Sun, Q. Song, X. Wang, Investigating the potential for self-healing aggregates in concrete, Constr. Build. Mater. 409 (2023) 133918.
[14] Y. Javeed, Y. Goh, K.H. Mo, S.P. Yap, B.F. Leo, Microbial self-healing in concrete: a comprehensive exploration of bacterial viability, implementation techniques, and mechanical properties, J. Mater. Res. Technol. 29 (2024) 2376–2395.
[15] M.A. Reda, S.E. Chidiac, Performance of capsules in self-healing early-age concrete due to restrained shrinkage, Constr. Build. Mater. 436 (2024) 136984.
[16] Z. Tang, B. Cao, C. Litina, V. Afroughsabet, C. Vlachakis, A. Al-Tabbaa, Development of novel self-healing strain-hardening cementitious composites (SH2CC) for dynamic cyclic loading conditions using mineral and polymer admixtures, Cem. Concr. Compos. 142 (2023) 105172.
[17] K.S. Lauch, J.P. Charron, C. Desmettre, Comprehensive evaluation of self-healing of concrete with different admixtures under laboratory and long-term outdoor expositions, J. Build. Eng. 54 (2022) 104661.
[18] H. Chang, C. Li, J. Wang, H. Zhang, Z. Ge, Z. Zuo, J. Liu, Y. Zhou, The features of different mineral admixtures affecting the self-healing capacity of cementitious-based materials, Constr. Build. Mater. 297 (2021) 123822.
[19] X. Lin, W. Li, A. Castel, T. Kim, Y. Huang, K. Wang, A comprehensive review on self-healing cementitious composites with crystalline admixtures: design, performance and application, Constr. Build. Mater. 409 (2023) 134108.
[20] E. Tsampali, M. Stefanidou, The role of crystalline admixtures in the long-term healing process of fiber-reinforced cementitious composites (FRCC), J. Build. Eng. 60 (2022) 105164.
[21] Y. Wang, X. Fan, R. Wu, H. Lin, W. Feng, Experimental study on long-term impermeability of recycled aggregate concrete mixed with crystalline admixture and waste glass powder, J. Clean. Prod. 458 (2024) 142551.
[22] V.G. Cappellesso, T. Van Mullem, E. Gruyaert, K. Van Tittelboom, N. De Belie, Self-healing concrete with a bacteria-based or crystalline admixture as healing agent to prevent chloride ingress and corrosion in a marine environment, Dev. Built Environ. (2024) 100486.
[23] Y. Ding, Z. Wu, Q. Huang, Q. Wang, Q. Ren, Z. Zhang, J. Zhang, K. Huang, Research on crystalline admixtures for low carbon buildings based on the self-healing properties of concrete, Constr. Build. Mater. 409 (2023) 133932.
[24] A.G. Borçato, R.A. Medeiros-Junior, Self-healing in metakaolin-based geopolymers with crystalline admixture, expansive agent, and hydrated lime, Constr. Build. Mater. 418 (2024) 135391.
[25] T. Evangelia, V. Ioanna, M. Stefanidou, Effect of hemp fibers and crystalline admixtures on the properties and self-healing efficiency of lime and clay-based mortars, J. Build. Eng. 86 (2024) 108963.
[26] V. Cappellesso, L. Ferrara, E. Gruyaert, K. Van Tittelboom, N.De Belie, Resilient crystalline admixture in ultra-high performance self-healing concrete under cyclic freeze-thaw with de-icing salts, Cem. Concr. Res. 181 (2024) 107524.
[27] Y. Chen, S. Li, B. Mezari, E.J. Hensen, R. Yu, K. Schollbach, H. Brouwers, Q. Yu, Effect of highly dispersed colloidal olivine nano-silica on early age properties of ultra-high performance concrete, Cem. Concr. Compos. 131 (2022) 104564.
[28] T. Liu, Y. Chen, B. Yuan, W. Zhuang, H.J.H. Brouwers, Q. Yu, Sodium aluminate activated waste glass: reduced efflorescence behavior by C(N)−A−S−H transformation, Cem. Concr. Res. 181 (2024) 107527.
[29] T. Liu, Analysis of Performance and Function of Composition of Cementitious Capillary Crystalline Waterproof Materials, Tsinghua University: Beijing, China (2011).
[30] X. Hu, J. Xiao, Z. Zhang, C. Wang, C. Long, L. Dai, Effects of CCCW on properties of cement-based materials: a review, J. Build. Eng. 50 (2022) 104184.
[31] W. Li, B. Dong, Z. Yang, J. Xu, Q. Chen, H. Li, F. Xing, Z. Jiang, Recent advances in intrinsic self-healing cementitious materials, Adv. Mater. 30 (17) (2018) 1705679.
[32] B. Joa, M.A. Sikandar, Z. Baloch, R.A. Khan, Effect of incorporation of self healing admixture (SHA) on physical and mechanical properties of mortars, J. Ceram. Process. Res 16 (2015) s138–s143.

[33] C. Xue, W. Li, Z. Luo, K. Wang, A. Castel, Effect of chloride ingress on self-healing recovery of smart cementitious composite incorporating crystalline admixture and MgO expansive agent, Cem. Concr. Res. 139 (2021) 106252.
[34] C. Xue, Performance and mechanisms of stimulated self-healing in cement-based composites exposed to saline environments, Cem. Concr. Compos. 129 (2022) 104470.
[35] R. Wang, Z. Ding, Y. Zhang, Y. Xu, Self-healing of high-performance engineered cementitious materials with crystalline admixture in the seawater environment, J. Build. Eng. (2022) 105472.
[36] C. Xue, Cracking and autogenous self-healing on the performance of fiber-reinforced MgO-cement composites in seawater and NaCl solutions, Constr. Build. Mater. 326 (2022) 126870.
[37] L. Ferrara, V. Krelani, M. Carsana, A "fracture testing" based approach to assess crack healing of concrete with and without crystalline admixtures, Constr. Build. Mater. 68 (2014) 535–551.
[38] K. Aspiotis, K. Sotiriadis, A. Ntaska, P. Mácová, E. Badogiannis, S. Tsivilis, Durability assessment of self-healing in ordinary portland cement concrete containing chemical additives, Constr. Build. Mater. 305 (2021) 124754.
[39] S. Indhumathi, A. Dinesh, M. Pichumani, Diverse perspectives on self healing ability of engineered cement composite–all-inclusive insight, Constr. Build. Mater. 323 (2022) 126473.
[40] C. Zhang, X. Guan, J. Li, Y. Li, R. Lu, Coupling effect of cementitious capillary crystalline waterproof material and exposure environments on self-healing properties of engineered cementitious composites (ECC), J. Build. Eng. 63 (2023) 105471.
[41] Z. Jiang, W. Li, Z. Yuan, Influence of mineral additives and environmental conditions on the self-healing capabilities of cementitious materials, Cem. Concr. Compos. 57 (2015) 116–127.
[42] X. Lin, A. Castel, Z. Deng, B. Dong, X. Zhang, S. Zhang, W. Li, Effect of crystalline admixtures on shrinkage and alkali-silica reaction of biochar-cementitious composites, Dev. Built Environ. 18 (2024) 100456.
[43] P. Azarsa, R. Gupta, A. Biparva, Assessment of self-healing and durability parameters of concretes incorporating crystalline admixtures and portland limestone cement, Cem. Concr. Compos. 99 (2019) 17–31.
[44] E. Cuenca, L. Ferrara, Pull-out tests to evaluate the effects of crack healing on the steel-to-concrete bond on concretes exposed to chloride-rich environments, J. Build. Eng. 75 (2023) 106933.
[45] H. Doostkami, M. Roig-Flores, P. Serna, Self-healing efficiency of ultra high-performance fiber-reinforced concrete through permeability to chlorides, Constr. Build. Mater. 310 (2021) 125168.
[46] J. Michael, S.H. Smith, S.A. Durham, M.G. Chorzepa, Crack control in concrete walls through novel mixture design, full-scale testing, and finite element analysis, Constr. Build. Mater. 166 (2018) 301–314.
[47] S. Afroz, Q.D. Nguyen, Y. Zhang, T. Kim, A. Castel, Evaluation of cracking potential parameters for low to high grade concrete with fly ash or slag, Constr. Build. Mater. 350 (2022) 128891.
[48] D.K. Nayak, P.P. Abhilash, R. Singh, R. Kumar, V. Kumar, Fly ash for sustainable construction: a review of fly ash concrete and its beneficial use case studies, Clean. Mater. 6 (2022) 100143.
[49] J. Xu, P. Zhan, W. Zhou, J. Zuo, S.P. Shah, Z. He, Design and assessment of eco-friendly ultra-high performance concrete with steel slag powder and recycled glass powder, Powder Technol. 419 (2023) 118356.
[50] P. Zhan, J. Xu, J. Wang, J. Zuo, Z. He, Structural supercapacitor electrolytes based on cementitious composites containing recycled steel slag and waste glass powders, Cem. Concr. Compos. 137 (2023) 104924.
[51] X. Lin, W. Li, Y. Guo, W. Dong, A. Castel, K. Wang, Biochar-cement concrete toward decarbonisation and sustainability for construction: characteristic, performance and perspective, J. Clean. Prod. 419 (2023) 138219.
[52] T. Chen, L. Zhao, X. Gao, L. Li, L. Qin, Modification of carbonation-cured cement mortar using biochar and its environmental evaluation, Cem. Concr. Compos. 134 (2022) 104764.
[53] X. Zhu, Y. Zhang, L. Chen, L. Wang, B. Ma, J. Li, C.S. Poon, D.C.W. Tsang, Bonding mechanisms and micro-mechanical properties of the interfacial transition zone (ITZ) between biochar and paste in carbon-sink cement-based composites, Cem. Concr. Compos. 139 (2023) 105004.
[54] C.S.R. Thimmareddy, A.R. Theja, C. Sashidhar, Self-healing ability of high-strength fibre-reinforced concrete with fly ash and crystalline admixture, Civ. Eng. J. 4 (2018) 971.
[55] G. Li, S. Liu, M. Niu, Q. Liu, X. Yang, M. Deng, Effect of granulated blast furnace slag on the self-healing capability of mortar incorporating crystalline admixture, Constr. Build. Mater. 239 (2020) 117818.
[56] R. Liu, H. Wang, H. Xiao, J. Li, P. Pan, W. Yang, Design method of high transport performance biochar-cement based materials based on particle size distribution and permeation probability calculation model, Constr. Build. Mater. 411 (2024) 134557.
[57] Y. Tang, J. Qiu, CO2-sequestering ability of lightweight concrete based on reactive magnesia cement and high-dosage biochar aggregate, J. Clean. Prod. 451 (2024) 141922.
[58] W. Xu, Y. Zhang, M. Li, F. Qu, C.S. Poon, X. Zhu, D.C.W. Tsang, Durability and micromechanical properties of biochar in biochar-cement composites under marine environment, J. Clean. Prod. 450 (2024) 141842.
[59] D. Kalderis, E. Anastasiou, E. Petrakis, S. Konopisi, Utilization of biochar from olive tree pruning as additive to cement mortars, J. Clean. Prod. 469 (2024) 143137.
[60] F. Qu, Y. Zhang, X. Zhu, W. Xu, C.S. Poon, W. Li, D.C.W. Tsang, Roles of wood waste biochar for chloride immobilization in GGBS-blended cement composites, Constr. Build. Mater. 411 (2024) 134389.
[61] A.S.f. Testing, M.C.C.-o. Cement, ASTM C348-21: Standard Test Method for Flexural Strength of Hydraulic-Cement Mortars, ASTM International, 2013.
[62] A. International, ASTM C349-18. Standard Test Method For Compressive Strength Of Hydraulic-Cement Mortars (Using Portions Of Prisms Broken In Flexure), ASTM International, United States of America, 2018.
[63] C. Xue, W. Li, F. Qu, Z. Sun, S.P. Shah, Self-healing efficiency and crack closure of smart cementitious composite with crystalline admixture and structural polyurethane, Constr. Build. Mater. 260 (2020) 119955.
[64] J. Li, X. Guan, Pretreated lightweight aggregates for self-healing concrete exposed to calcium hydroxide-rich sewage, Constr. Build. Mater. 365 (2023) 130117.
[65] L. Ferrara, T. Van Mullem, M.C. Alonso, P. Antonaci, R.P. Borg, E. Cuenca, A. Jefferson, P.-L. Ng, A. Peled, M. Roig-Flores, M. Sanchez, C. Schroefl, P. Serna, D. Snoeck, J.M. Tulliani, N.De Belie, Experimental characterization of the self-healing capacity of cement based materials and its effects on the material performance: a state of the art report by COST action SARCOS WG2, Constr. Build. Mater. 167 (2018) 115–142.
[66] P. Li, W. Li, K. Wang, J.L. Zhou, A. Castel, S. Zhang, S.P. Shah, Hydration of portland cement with seawater toward concrete sustainability: phase evolution and thermodynamic modelling, Cem. Concr. Compos. 138 (2023) 105007.
[67] P. Zhan, J. Wang, H. Zhao, W. Li, S.P. Shah, J. Xu, Impact of synthetic C-S-H seeds on early hydration and pore structure evolution of cement pastes: a study by 1H low-field NMR and path analysis, Cem. Concr. Res. 175 (2024) 107376.
[68] L. Chen, Y. Zhang, L. Wang, S. Ruan, J. Chen, H. Li, J. Yang, V. Mechtcherine, D. C.W. Tsang, Biochar-augmented carbon-negative concrete, Chem. Eng. J. 431 (2022) 133946.
[69] H. Zhao, W. Li, Y. Gan, K. Wang, Z. Luo, Nano/microcharacterization and image analysis on bonding behaviour of ITZs in recycled concrete enhanced with waste glass powder, Constr. Build. Mater. 392 (2023) 131904.
[70] K. Kurumisawa, T. Nawa, H. Owada, M. Shibata, Deteriorated hardened cement paste structure analyzed by XPS and 29Si NMR techniques, Cem. Concr. Res. 52 (2013) 190–195.
[71] I.G. Richardson, Tobermorite/jennite- and tobermorite/calcium hydroxide-based models for the structure of C-S-H: applicability to hardened pastes of tricalcium silicate, β-dicalcium silicate, portland cement, and blends of Portland cement with blast-furnace slag, metakaolin, or silica fume, Cem. Concr. Res. 34 (9) (2004) 1733–1777.
[72] S. Meng, Z. Shi, X. Ouyang, Comparison of the effects of carbon-based and inorganic nanomaterials on early cement hydration, Constr. Build. Mater. 421 (2024) 135705.
[73] L. Wang, G. Zhang, P. Wang, S. Yu, Effects of fly ash and crystalline additive on mechanical properties of two-graded roller compacted concrete in a high RCC arch dam, Constr. Build. Mater. 182 (2018) 682–690.
[74] S. Gupta, H.W. Kua, Effect of water entrainment by pre-soaked biochar particles on strength and permeability of cement mortar, Constr. Build. Mater. 159 (2018) 107–125.
[75] M.Haris Javed, M. Ali Sikandar, W. Ahmad, M. Tariq Bashir, R. Alrowais, M. Bilal Wadud, Effect of various biochars on physical, mechanical, and microstructural characteristics of cement pastes and mortars, J. Build. Eng. 57 (2022) 104850.
[76] X. Wang, S. Chen, J. Ren, R. Huang, Z. Yang, W. Wang, J. Liu, Effect of super absorbent polymer and mineral additives on mechanical, shrinkage and healing properties of self-healing lightweight aggregate concrete under different curing regimes, Constr. Build. Mater. 357 (2022) 129377.
[77] E. Cuenca, A. Mezzena, L. Ferrara, Synergy between crystalline admixtures and nano-constituents in enhancing autogenous healing capacity of cementitious composites under cracking and healing cycles in aggressive waters, Constr. Build. Mater. 266 (2021) 121447.
[78] X. Guan, C. Zhang, Y. Li, S. Zhao, Effect of exposure conditions on self-healing behavior of engineered cementitious composite incorporating limestone powder, Cem. Concr. Compos. 114 (2020) 103808.
[79] T. Van Mullem, E. Gruyaert, B. Debbaut, R. Caspeele, N. De Belie, Novel active crack width control technique to reduce the variation on water permeability results for self-healing concrete, Constr. Build. Mater. 203 (2019) 541–551.
[80] K. Van Tittelboom, E. Gruyaert, H. Rahier, N. De Belie, Influence of mix composition on the extent of autogenous crack healing by continued hydration or calcium carbonate formation, Constr. Build. Mater. 37 (2012) 349–359.
[81] A. de Souza Oliveira, R.D. Toledo Filho, E. de Moraes Rego Fairbairn, L.F.C. de Oliveira, O. da Fonseca Martins Gomes, Microstructural characterization of self-healing products in cementitious systems containing crystalline admixture in the short- and long-term, Cem. Concr. Compos. 126 (2022) 104369.
[82] M. De Rooij, K. Van Tittelboom, N. De Belie, E. Schlangen, Self-healing phenomena in cement-Based materials: state-of-the-art report of RILEM technical committee 221-SHC. self-Healing phenomena in cement-Based materials, Springer, 2013.
[83] C. Xue, M.J. Tapas, V. Sirivivatnanon, Cracking and stimulated autogenous self-healing on the sustainability of cement-based materials: a review, J. Sustain. Cem. -Based Mater. 12 (2) (2023) 184–206.
[84] K. Sisomphon, O. Copuroglu, E.A.B. Koenders, Self-healing of surface cracks in mortars with expansive additive and crystalline additive, Cem. Concr. Compos. 34 (4) (2012) 566–574.
[85] K.S. Lauch, C. Desmettre, J.P. Charron, New water permeability set-up and factors affecting concrete self-healing, Constr. Build. Mater. 294 (2021) 123595.

[86] A.S. Buller, Fu.R. Abro, K.-M. Lee, S.Y. Jang, Mechanical recovery of cracked fiber-reinforced mortar incorporating crystalline admixture, expansive agent, and geomaterial, Adv. Mater. Sci. Eng. 2019 (1) (2019) 3420349.
[87] W. Tian, Y. Liu, W. Wang, Multi-structural evolution of conductive reactive powder concrete manufactured by enhanced ohmic heating curing, Cem. Concr. Compos. 123 (2021) 104199.
[88] L. Ferrara, N. Ozyurt, M. di Prisco, High mechanical performance of fibre reinforced cementitious composites: the role of "casting-flow induced" fibre orientation, Mater. Struct. 44 (1) (2011) 109–128.
[89] L. Restuccia, A. Reggio, G.A. Ferro, R. Kamranirad, Fractal analysis of crack paths into innovative carbon-based cementitious composites, Theor. Appl. Fract. Mech. 90 (2017) 133–141.
[90] H. Li, Y. Wu, A. Zhou, C. Zhao, L. Deng, F. Lu, Experimental study on self-healing performance of tunnel lining concrete based on response surface methodology, Constr. Build. Mater. 425 (2024) 136105.
[91] Q. Fu, S. Zhang, J. Zhou, J. Wang, X. Wang, Q. Huang, L. Lu, The synergistic effect of microorganisms and multiple admixtures on improving the self-healing of cracks in biogenic mortar exposed to different marine environments, Constr. Build. Mater. 423 (2024) 135884.
[92] J. Qiu, H.S. Tan, E.-H. Yang, Coupled effects of crack width, slag content, and conditioning alkalinity on autogenous healing of engineered cementitious composites, Cem. Concr. Compos. 73 (2016) 203–212.
[93] B. Vafaei, A. Ghahremaninezhad, Self-healing effect of hydrogels in cement slag and fly ash pastes, Constr. Build. Mater. 438 (2024) 137036.
[94] D.H. Chu, M. Vinoba, M. Bhagiyalakshmi, I.I. Hyun Baek, S.C. Nam, Y. Yoon, S. H. Kim, S.K. Jeong, CO2 mineralization into different polymorphs of CaCO3 using an aqueous-CO2 system, RSC Adv. 3 (44) (2013) 21722–21729.
[95] I. García Lodeiro, D.E. Macphee, A. Palomo, A. Fernández-Jiménez, Effect of alkalis on fresh C–S–H gels. FTIR analysis, Cem. Concr. Res. 39 (3) (2009) 147–153.
[96] M. Yousuf, A. Mollah, T.R. Hess, Y.-N. Tsai, D.L. Cocke, An FTIR and XPS investigations of the effects of carbonation on the solidification/stabilization of cement based systems-Portland type V with zinc, Cem. Concr. Res. 23 (4) (1993) 773–784.
[97] F. Souayfan, E. Rozière, M. Paris, D. Deneele, A. Loukili, C. Justino, 29Si and 27Al MAS NMR spectroscopic studies of activated metakaolin-slag mixtures, Constr. Build. Mater. 322 (2022) 126415.
[98] A.F. Jamsheer, K. Kupwade-Patil, O. Büyüköztürk, A. Bumajdad, Analysis of engineered cement paste using silica nanoparticles and metakaolin using 29Si NMR, water adsorption and synchrotron X-ray Diffraction, Constr. Build. Mater. 180 (2018) 698–709.
[99] P. Colombet, A.-R. Grimmer, H. Zanni, P. Sozzani, Nuclear magnetic resonance spectroscopy of cement-based materials, Springer Science & Business Media, 2012.
[100] M.E. Krüger, H. Hilbig, L. Stelzner, A. Machner, Effect of the chemical composition of synthetic alkali-silica gels on their structure, swelling behavior and water uptake, Cem. Concr. Res. 184 (2024) 107596.
[101] M.E. Krüger, A. Heisig, H. Hilbig, H. Eickhoff, D. Heinz, A. Machner, Effect of aluminum on the structure of synthetic alkali-silica gels, Cem. Concr. Res. 166 (2023) 107088.
[102] C.M. Tibbetts, K.A. Riding, C.C. Ferraro, A critical review of the testing and benefits of permeability-reducing admixtures for use in concrete, Cement 6 (2021) 100016.
[103] X.F. Wang, Z.H. Yang, C. Fang, N.X. Han, G.M. Zhu, J.N. Tang, F. Xing, Evaluation of the mechanical performance recovery of self-healing cementitious materials – its methods and future development: a review, Constr. Build. Mater. 212 (2019) 400–421.
[104] T.S.R. Chandra, A. Ravitheja, Macro mechanical properties of self healing concrete with crystalline admixture under different environments, Ain Shams Eng. J. 10 (1) (2019) 23–32.
[105] S.S. Lucas, M. von Tapavicza, A.M. Schmidt, J. Bertling, A. Nellesen, Study of quantification methods in self-healing ceramics, polymers and concrete: a route towards standardization, J. Intell. Mater. Syst. Struct. 27 (19) (2016) 2577–2598.